Multimodal Characterization of a Linear DNA-Based Nanostructure

Susan Buckhout-White,[†,⊥] Mario Ancona,[§] Eunkeu Oh,[‡,#] Jeffrey R. Deschamps,[†] Michael H. Stewart,[‡] Juan B. Blanco-Canosa,[∥] Philip E. Dawson,[∥] Ellen R. Goldman,[†] and Igor L. Medintz[†,*]

[†]Center for Bio/Molecular Science and Engineering, Code 6900, [‡]Optical Sciences Division, Code 5611, and [§]Electronic Science and Technology Division, Code 6876, U.S. Naval Research Laboratory, Washington, D.C. 20375, United States, [⊥]George Mason University, 10910 University Blvd, MS 4E3, Manassas, Virginia 20110, United States, [∥]Departments of Cell Biology and Chemistry, The Scripps Research Institute, La Jolla, California 92037, United States, and [#]Sotera Defense Solutions, Crofton, Maryland 21114, United States

ABSTRACT Designer DNA structures have garnered much interest as a way of assembling novel nanoscale architectures with exquisite control over the positioning of discrete molecules or nanoparticles. Exploiting this potential for a variety of applications such as light-harvesting, molecular electronics, or biosensing is contingent on the degree to which various nanoarchitectures with desired molecular functionalizations can be realized, and this depends critically on characterization. Many techniques exist for analyzing DNA-organized nanostructures; however, these are almost never used in concert because of overlapping concerns about their differing character, measurement environments, and the disparity in DNA modification chemistries and probe structure or size. To assess these concerns and to see what might be gleaned from a multimodal characterization, we intensively study a single DNA nanostructure using a multiplicity of methods. Our test bed is a linear 100 base-pair double-stranded DNA that has been modified by a variety of chemical handles, dyes, semiconductor quantum dots, gold nanoparticles, and electroactive labels. To this we apply a combination of physical/optical characterization methods including electrophoresis, atomic force microscopy, transmission electron microscopy, dynamic light scattering, Förster resonance energy transfer, voltammetry, and structural modeling. In general, the results indicate that the differences among the techniques are not so large as to prevent their effective use in combination, that the data tend to be corroborative, and that differences observed among them can actually be quite informative.

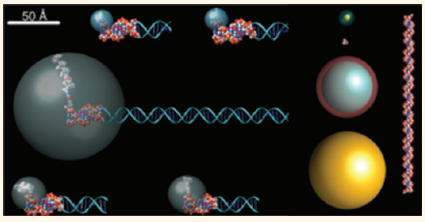

KEYWORDS: DNA · AFM · TEM · voltammetry · FRET · DLS · characterization · gold nanoparticles · fluorophore · Os-bipy · semiconductor · metrology · quantum dot · electrophoresis · modeling

Developing methods for patterning discrete particles and molecules at the nanoscale has become an important avenue for nanotechnological research as the limitations and inefficiencies of conventional top-down patterning become ever more apparent. For such work, investigators are increasingly turning to self-assembly methodologies. While there are many systems that allow for self-assembly of simple molecular structures, DNA-based technologies provide inherent advantages due to the precise nature of Watson–Crick base pairing and the molecular-level control one has over base sequence. In the simplest examples, linear DNA constructs have been assembled with a wide variety of particle and molecular attachments including fluorescent dyes, semiconductor quantum dots (QDs), gold nanoparticles (AuNPs), and proteins, clearly demonstrating the potential of DNA functionalization chemistry for nanoscale control.[1−4] Greatly expanding the potential application space, Seeman pioneered methods that use DNA as a self-assembled structural material.[5] As he elegantly demonstrated, the use of crossovers, tiles, and junctions permits a wide range of structures to be realized.[6−10] Rothemund extended this methodology further with DNA origami,[11] an approach for creating arbitrary two-dimensional DNA structures using a long scaffold strand and many smaller staple strands.[12−16] In all implementations, since each base or set of bases within the DNA structure is uniquely addressable, there is potential for a self-assembly approach that allows for arbitrary particle or molecular placement with a resolution approaching the base-to-base separation distance of ~3 Å.

In order to reach a full understanding of the accuracy with which such DNA structures form and the consequent precision that can be realized in DNA-based patterning, it is necessary to examine a variety of assembled structures in intimate detail using a diverse set of techniques. To date, such a study has not been performed, nor is it clear what exactly would constitute a "full" characterization. In molecular biology, X-ray crystallography is the gold standard in dimensional characterization, and in the DNA structural area this method has been used

* Address correspondence to Igor.medintz@nrl.navy.mil.

Received for review June 20, 2011 and accepted January 3, 2012.

Published online January 18, 2012
10.1021/nn204680r

occasionally, with perhaps the most notable example being Seeman's recent work with 3-D structures.[17] This method has not (yet) proven of much value for functionalized or other complex DNA structures, in part because of the often-severe challenges of obtaining the requisite crystals and because its information would be incomplete; for example, it would not provide dimensional characterization of structures in solution. At present the workhorse method for characterizing DNA assemblies, particularly for 2D structures such as those based on origami, is atomic force microscopy (AFM).[9,10,13−16,18,19] AFM does provide a good measure of the topography of the sample, but it cannot distinguish between different materials, such as DNA and AuNPs. Moreover, since it involves the use of a stylus of finite curvature, its lateral resolution is limited to a few nanometers at best. Direct visualization methods such as transmission electron microscopy (TEM) and scanning electron microscopy (SEM) can provide complementary types of information but are typically less capable of imaging the DNA itself, unless special staining is introduced to increase contrast.[13] Imaging with these methods also generally requires mounting the sample on a surface, which likely alters the conformation of the DNA and its attached particles.[20] For sampling in solution, direct imaging is not usually feasible, but dimensional characterization is still achievable using spectroscopy and, in particular, by monitoring Förster resonance energy transfer (FRET) between chromophores attached to the DNA. Many studies of DNA utilizing FRET have been reported in the literature, although typically it is used in a stand-alone mode as a spatial characterization method.[1,6,7,19,21]

More pertinently, the aforementioned techniques have almost never been used in concert because of overlapping concerns about their differing measurement environments (*e.g.*, dry *versus* aqueous), multiple DNA modification chemistries (*e.g.,* amines, thiols, or biotin) or labels (*e.g.*, dyes *versus* QDs or AuNPs), and probing modalities (*e.g.*, spectroscopic *versus* microscopic). Moreover, little work is currently available that directly compares DNA modifications for probe labeling. The present report is motivated by the notion that a single characterization approach provides only a limited window for investigating functionalized DNA assemblies. We suggest that many of these techniques may actually provide corroborating and/or complementary information and that significantly more information is available, especially concerning subtle or dynamic structural details, by exploiting a multimodal characterization approach that targets both the assembly process and the final structure itself.

Our goal here is to systematically apply a wide range of characterization techniques including electrophoresis, AFM, TEM, dynamic light scattering (DLS), FRET, voltammetry, and structural modeling to a model DNA structure. Analysis of the results allows us to evaluate the different measurement techniques along with the information derived therein and to assess the effects of the DNA modifications and labels including dyes, QDs, AuNPs, and electroactive labels on the comparative analysis. For each technique utilized, the particle or molecule attached to the DNA was chosen for its optimal performance in terms of signal or contrast, *e.g.*, AuNPs for TEM and AFM studies along with fluorescent dyes or QDs for FRET studies. We further examine each technique for its ability to monitor initial stepwise structural assembly, the precision with which point functionalization(s) in the DNA structures can be assessed, and how all of the techniques compare in terms of overall information provided. With an understanding of what these techniques offer and how they can be applied in concert, a more thorough overall appreciation of functionalized DNA systems, their dynamic nature, and especially the subtleties within them can be attained.

RESULTS

DNA Sequences. The goal of this work was to characterize a single DNA nanostructure using a wide array of analytical techniques. An important part of the analysis compared the data derived from the different techniques, and we thus required a DNA assembly that would maintain its intrinsic structure in many different environments and after undergoing a variety of modifications and labelings. To meet this requirement and allow for accurate comparisons, we selected a simplified, rigid-linear architecture encompassing a 100 base-pair (bp) segment of double-stranded (ds) linear DNA. The underlying structure consisted of a single-stranded (ss) DNA backbone or template paired with 3-complementary oligos, each one-third the length of the backbone, which simultaneously served to provide a regular spacing and separation for a variety of attached labels. For certain experiments, a contiguous 100 bp complement to the backbone was also used. Hybridization was used to assemble either the full structure or partial iterations thereof in all the different analyses implemented.

Figure 1 depicts the backbone and the positioning of the complementary segments of DNA (referred to as A, B, or C) along with the modifications introduced to allow facile attachment of the desired labels. The sequences were chosen so that there are no more than 8 bases of self-complementarity within the backbone or the complements, helping to ensure that no unintended secondary structures could form. Furthermore, the sequences of the complementary pieces were designed to have no more than 6 bases of complementarity to the backbone in locations other than the intended target, again to drive the formation of the desired hybridized structure. Given the length of

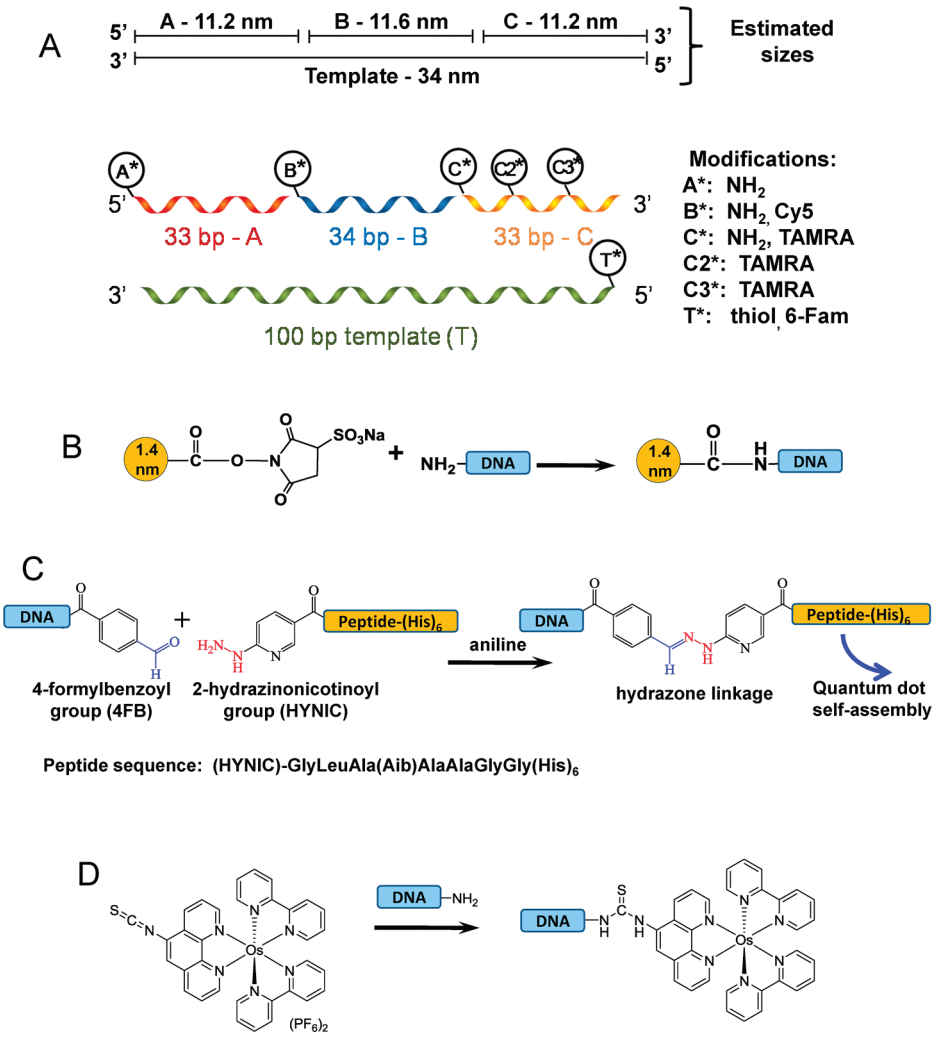

Figure 1. DNA schematic and chemoselective ligation. (A) Schematic of the DNA sequences; a 100 bp template with 33, 34, and 33 bp complements, A, B, and C. Subsequent functionalization to specific sequences and locations utilized the various modifiers shown on the right. (B) NHS-reaction used to attach the amine-modified DNA to the monolabeled sulfo-NHS Nanogold. (C) Aniline-catalyzed hydrazone ligation between the aldehyde (blue) of the 4FB group and the peptidyl-HYNIC group (red) used to link DNA to the $(His)_6$-peptide. (D) Reaction of the osmium isothiocyanate with the amine-modified DNA to form the Os—DNA conjugate. Note, the DNA-linked OS has a 2^+ charge which is not shown.

one base pair of DNA, 0.34 nm for the expected B-DNA form, the lengths for the corresponding oligos are estimated to be (A) 11.2, (B) 11.6, and (C) 11.2 nm, respectively, with the total length of the hybridized, ds-nicked DNA strand being 34 nm. To predict the expected distances between the DNA segments and point functionalizations as well as the overall length, it is necessary that the structure remain essentially linear. The persistence length of dsDNA is roughly 50 nm or 150 bp,[22] and so we expect our 34 nm DNA segment to exist in an extended state. It is possible, however, that having nicks in the DNA could disrupt the base stacking and lead to bending of the overall structure, thereby affecting the length of the DNA strand. On the basis of the work of Furrer, the persistence length of highly nicked DNA in a comparable salt concentration buffer was reported to be 43 nm,[23] which again suggests linear behavior for our 34 nm DNA. Stacking instability is also reported to be sequence dependent,[24] with a nick between the thymine and adenine bases when oriented 5′—3′ being the most susceptible to instability. This sequence pair does occur in our construct between the A and B segments and may result in some bending or flexing at this point. Despite this uncertainty it should be noted that such bending will not affect the linearity of the DNA between adjacent segments. Consequently, measurements from adjacent functionalization points can still be judged against the expected linear distance of the DNA. Moreover, with this linearity assumption, deviations from the expected estimate can be attributed to the flexibility of the attachment ligand, *i.e.*, peptide or dye linkers used, and to the efficiency of the attachment, *i.e.*, if the desired nanoparticle/molecule has indeed attached.

DNA Modifications and Labeling. The wide range of analytical techniques applied here required functionalizing the DNA with many different probes, which, in turn, required selectively modifying the DNA sequences with either dyes directly or various chemical handles that served as linkers for the subsequent attachment of a probe. The DNA was thus obtained modified, as per Figure 1, with terminal amine and thiol groups or with Cy5, TAMRA, or 6-FAM dye probes; the latter were incorporated during synthesis. All of these modifications were located at the DNA's 5′-end, except the TAMRA dyes, which were sometimes placed internally in oligo C.

The amine modification was used as the site for labeling with *sulfo-N*-hydroxysuccinimide (NHS)-activated 1.4 nm AuNPs for AFM and TEM analysis, with a reactive osmium isothiocyanate (OsICN) molecule for electrochemical analysis or with an NHS-activated 4-formylbenzoyl group (4FB). Once functionalized with 4FB, the DNA was chemoselectively ligated to a peptide displaying an N-terminal 2-hydrazinonicotinoyl (HYNIC) group and a C-terminal hexahistidine (His_6); the latter allows for metal-affinity coordination to QDs for FRET analysis. The thiol modification allowed for direct DNA chemisorption to the surface of citrate-stabilized 15 nm AuNPs for DLS analysis. Schematics of the selective attachment chemistries are shown in Figure 1B–D. Detailed descriptions of the labels, their syntheses (where applicable), their chemical attachments to the DNA, the approach to forming the DNA structures, and each method/analysis as applied here are provided in the subsequent Materials and Methods section. Chemical structures of the amine/thiol DNA modifications along with the dyes are given in the Supporting Information.

Structural Modeling of Modified DNA and Selected Probes. Given the variety of DNA modifications and probes used here, we wished to project *a priori* what potential impact their mass and extension might have. To accomplish this, we turned to structural modeling of the DNA modifications as a means of estimating the maximum rotational/extensional freedom for each along with its potential effects on the mass and size of the full DNA construct; see Materials and Methods for a full description. Figure 2A shows a series of representative images from this analysis. For all structures, except (iv), which shows the full 100 bp dsDNA for comparison purposes, a 10 bp ds-portion of the DNA's 5′-terminus is shown as a hybrid of a space-filling model superimposed over a stick and ribbon helix. The space-filling chemical structures (i)–(vii) are attached to the DNA and depict the thiol linker, amine linker, OsICN, His_6-peptide-HYNIC, Cy5, TAMRA, and 6-FAM, respectively. In comparison to the mass of the 100 bp ds template (61 660), the mass of the modifications, OsICN, or dyes ranges from 117 for the amine modification to 1560 for the His_6-peptide-HYNIC; see Table 1. This corresponds to a comparative value of 0.2–2.5% of the mass of the dsDNA structure, which is clearly insignificant. As the exact masses of the AuNP and QD probes are hard to estimate, these were not compared, although it is likely that their masses far exceed that of the full dsDNA structure. The gray spheres in Figure 2A represent the full range of rotation for each DNA attachment or modification assuming they are maximally extended. In reality, most will be far more compact due to steric and molecular considerations, and this is especially true for the His_6-peptide-HYNIC. The estimated maximum extension or length of each modification is also given in Table 1 along with a comparison to the dsDNA template. Excluding the QD/NP and dye materials, we see that these distances are relatively small and range from 3% to 6% of the size of the DNA, except for the His_6-peptide-HYNIC, which is slightly less than 20%.

Figure 2B provides a comparison of the size of the different probes utilized relative to that of the 100 bp DNA. This image includes the 1.4 nm AuNP, 6-FAM dye, QD, and 15 nm AuNP along with the 100 bp dsDNA displayed in a full space-filling representation. Again it is readily apparent that the dyes and even the 1.4 nm AuNP (shown with its ligand shell) contribute little to the overall size when attached to the DNA; all are less than <10% of the length. Given its small size, the same would also be true for the OsICN. In contrast, the large size of the 15 nm AuNPs and QDs approach 26% and 44% of the extension length of the DNA, respectively, which means that any analytical formats implementing these materials must take this fact into account. Overall, this analysis provides us with a quantitative basis for understanding the contributions of the modifications, linkers, and probes to the underlying DNA structure, and it allows us to estimate the minimum/maximum limits of probe movement. This is especially important for characterization methods such as FRET, where probe rotation plays a significant role (see below).

Electrophoresis. We began by confirming formation of the DNA structures following hybridization. The backbone was hybridized in three separate configurations: with just complementary segment A, with A and B, and with all three complementary oligos, A, B, and C. These constructs were then run side by side on a 2% agarose gel along with the unhybridized ss-backbone or template DNA for comparison purposes, as shown in Figure 3B. The clear stepwise differences in migration within the gel matrix indicate that each oligo is binding to the DNA backbone and results in an increasingly larger size, which matches expectations. In comparison, the backbone migrates at less than 50 bp in ss-form. Subsequent hybridization of each complement increases the size of the predominant band, with the full construct closely matching the expected size of ~100 bp dsDNA. Examination of the final hybridized structure shows that the majority of the DNA engaged

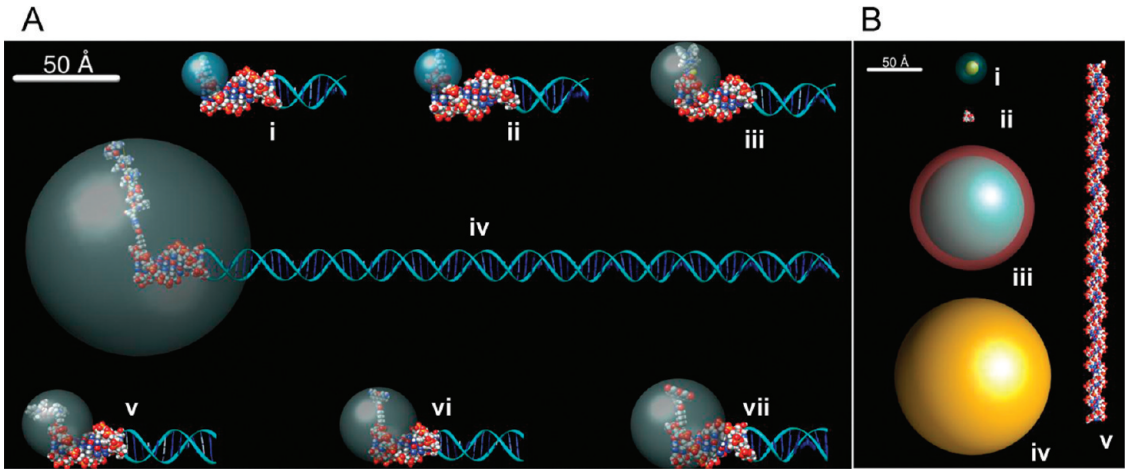

Figure 2. Modeling of DNA modifications and probes. (A) Model of the DNA structures appended with various modifications and probes. The gray spheres simulate the estimated maximum rotational extension of each at the DNA's terminus. The 10 bp portion of dsDNA is shown in a ribbon and stick hybrid structure terminating with a space-filling portion. Structures correspond to DNA appended with (i) thiol linker, (ii) amine linker, (iii) OsICN, (iv) His_6-peptide-HYNIC, (v) Cy5, (vi) TAMRA, and (vii) 6-FAM. The His_6-peptide-HYNIC is shown attached to a full DNA structure. (B) Comparison of scaled probe sizes. Structures shown correspond to (i) 1.4 nm AuNP (yellow) stabilized with a phosphine ligand (green), (ii) 6-FAM, (iii) 640 nm emitting QD (aqua) stabilized with DHLA ligand (red), (iv) 15 nm AuNP with no surface ligand, and (v) the ds 100 bp DNA. Complete chemical structures for modifications and dyes/probes are provided in Figure 1 and the Supporting Information.

TABLE 1. Estimated Molecular Weight and Length/Diameter of Selected Components

component	approximate MW[a]	estimated length/diameter[a]
dsDNA template	61 660	340 Å
C_6-thiol	134 (0.2)	10.1 Å (3)
amine-modification	117 (0.2)	9.8 Å (3)
His_6-peptide-HYNIC	1560 (2.5)	53 Å (17)
4-formylbenzoyl	150 (0.2)	8.2 Å (2.5)
6-FAM	475 (0.8)	19.8 Å (6)
OsICN	1030 (1.7)	16.3 Å (5)
1.4 nm AuNP		29.5 Å (9)[b]
15 nm AuNP		150 Å (44)
640 nm QD		80–100 Å (26)[c]

[a] Values in parentheses are percentage comparison to the dsDNA template mass/length. [b] Includes surface-stabilizing phosphene ligand. [c] Does not include the DHLA shell, as the His_6 interacts directly with the QD surface.

in the described hybridization and formed the full construct. The gel also shows that some residual unhybridized and/or partially hybridized DNA remains, a finding that is not surprising given the underlying assembly kinetics. For higher purity, one could excise the particular band of interest from the gel; however, this generally results in significant sample loss. Overall, the pattern of bands seen in Figure 3 serves as a basic confirmation that each increment along with the full 100 bp ds-structure has indeed formed and also sets a useful baseline for comparison with other DNA constructs.

TEM. Several papers have demonstrated that one can visualize DNA with TEM if the contrast is enhanced using staining with heavy metal ions or metal evaporation.[25–28] However, use of these enhancement methods can readily interfere with the subsequent visualization of attached particles by compromising the spatial resolution, especially when the particles are similar or smaller in size compared to the DNA backbone. Although this can be alleviated through the use of larger particles, such an approach sacrifices information about the location and flexibility of the attaching ligand. For these reasons, we chose instead to image the DNA unstained and relied on our ability to observe ultrasmall attached gold particles to provide the spatial resolution; specifically we used 1.4 nm diameter Nanogold (AuNP).

The AuNP-functionalized DNA construct shown schematically in Figure 3A was formed by first assembling the DNA with terminal amine modifications displayed at some or all of the 5′-ends of oligo segments A, B, and C. As described in the Methods section, these were then reacted with *mono* sulfo-NHS Nanogold (Nanoprobes.com), which is provided in a monovalent form, thereby favoring a 1:1 stoichiometric labeling on each available amine. Figure 3C shows a representative agarose gel of various AuNP-labeled assemblies, with no noticeable migration difference between assemblies labeled with 0, 1, 2, or 3 particles. This suggests that the added presence of the small and essentially neutral AuNPs does not affect the electrophoretic mobility appreciably (see Supporting Figure 1 for AuNP surface ligand structure).

For TEM visualization, the AuNP–DNA constructs were deposited on a holey carbon grid that had been pretreated with poly-L-lysine. Seen clearly in the TEM images of the fully occupied structure (Figure 3D) are distinct groups of three high-contrast spots, arranged linearly as associated with the high-*Z* AuNPs (we note that no DNA is apparent between the spots, an expected result given the lack of contrast). While there is nothing about positions A, B, and C that makes them individually distinguishable in the TEM, their relative

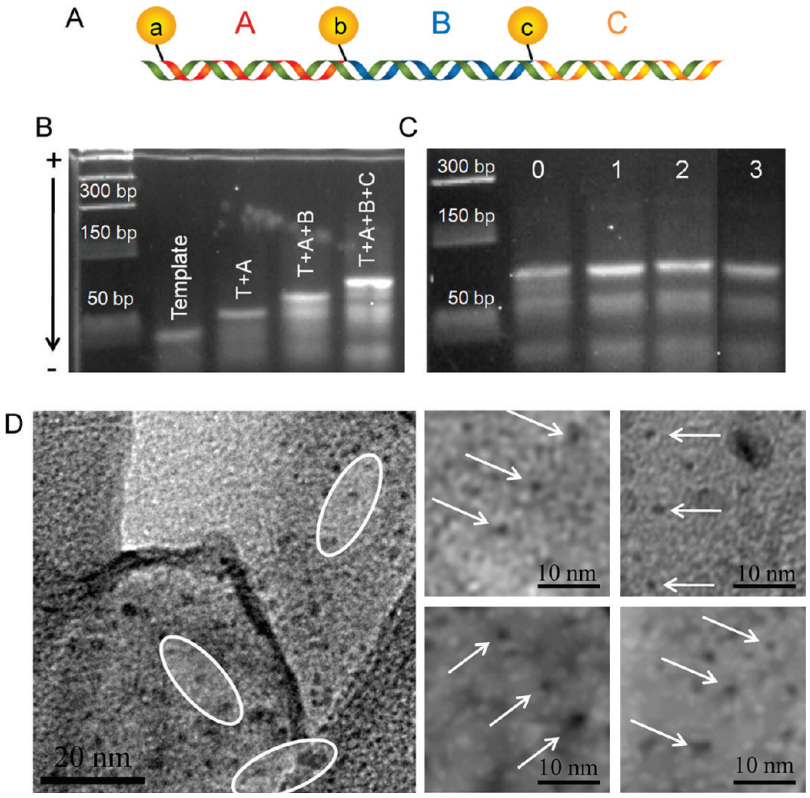

Figure 3. Nanogold-functionalized DNA for TEM. (A) Schematic of the DNA construct with one monolabeled NHS-Nanogold attached to the NH_2-modified 5′-end of each DNA complement. (B) A 3% agarose gel showing the hybridization of the unlabeled DNA structure. The gel clearly shows the stepwise migration with subsequent addition of each DNA complement, A, B, and C. (C) A 1% agarose gel showing the migration of increasing Au-attached DNA structures. The numbers 0−3 reflect the increasing number of amine-labeled labeled A, B, and C oligos prehybridized onto the backbone and then subjected to gold nanoparticle labeling. 0 reflects no amine and thus no gold, while 3 reflects all 3 present and thus a high probability of 3 AuNPs present. (D) TEM of DNA with 3-attached Nanogold particles. Inset shows a close-up of several representative Au−DNA structures.

locations can be easily determined. On the basis of the DNA structure alone, the separation between the AuNPs should be about 11.2/11.6 nm. However, the linker joining the gold to each DNA (Supporting Figure 1) should add another ±1 nm to this value, yielding expected values of 12.2/12.6 ± 1 nm. Statistical analysis of these structures in the representative TEM images shown in Figure 3D, as well as others, provided us with an average spacing of 10.0 ± 1.0 nm. We partially attribute the discrepancy in expected *versus* experimentally derived values (<20%) to the dehydration of the DNA structure in the high TEM vacuum environment and the fact that the gold may now be immobilized onto the DNA and not extending away from it in many cases.

AFM. As noted earlier, AFM is the most common technique used for visualizing DNA−particle conjugates, and its chief advantage is that it provides an accurate measure of the sample topography, particularly in the *z*-direction. With respect to the lateral dimensions, AFM is less precise, generally adding size to small particles due to convolution of the sample and tip topographies.[29] However, if the particles can be resolved, then relative distances can still be accurately gauged by focusing on the center-to-center distance. Given the close spacings involved in our work, it was imperative for us to employ ultrasharp tips; specifically we used special diamond-like carbon tips that have nominal radii of curvature of 1 nm.

The samples utilized for the AFM studies were the same Nanogold-labeled DNA as described above. The substrates were freshly cleaved mica, treated with $NiCl_2$, and imaged under dry conditions in tapping mode. From the representative results in Figure 4, it is clear that the attachment chemistry process does not successfully bind AuNPs to all of the amine groups present on the DNA. About one-third of the ~70 structures observed have all three sites occupied by gold particles. Structures missing one AuNP were evenly split between lacking an end or a center label, with representative examples shown in Figure 4B−E. As the figures show, AFM is similar to TEM in not being able to resolve the DNA itself, a finding we attribute to the short length of the DNA; when longer DNA is used, it does become clearly identifiable in the AFM images (not shown). In any event, based on direct measurements of all of the fully labeled structures (*i.e.*, each with three AuNPs), we obtain an average particle spacing of 11.3 nm with a standard deviation of 1.9 nm. Furthermore, an automated image analysis of the pair-correlation statistics (see Supporting Information

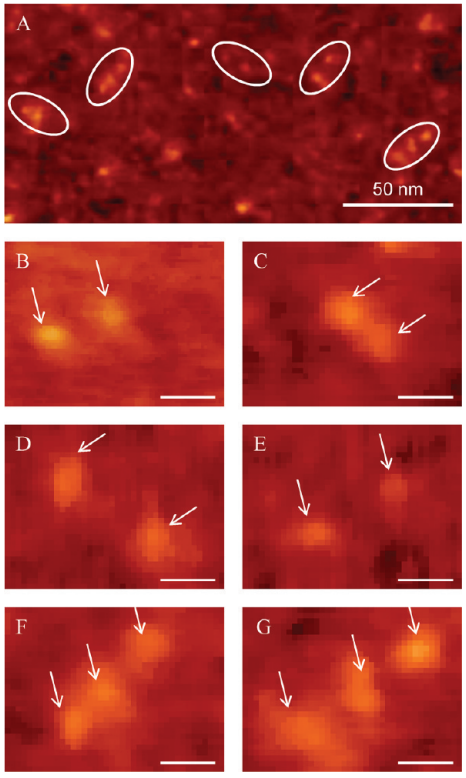

Figure 4. AFM of Nanogold-functionalized DNA. (A) AFM image with several of the DNA structures circled. (B, C) DNA labeled with AuNPs in two out of three adjacent positions. (D, E) DNA labeled in the two outer positions. (F, G) DNA labeled in all three available positions. Scale bars for B–G are 10 nm.

Figure S-2 for more detail) finds high probabilities for particles being 11.9 and 22.1 nm apart. This corresponds quite well with the expected distances of 11.2 and 22.4 nm (<10% difference) predicted from structural analysis for the closest and furthest separation distances of two AuNPs attached to the DNA, respectively. This agreement also suggests that the drying of the DNA in the AFM sample is only partial and not as significant as seen in the TEM sample.

DLS. This analytical technique usually provides a relatively quick and nondestructive method for gathering structural data on colloidal particulates in solution. Specifically, the method derives an averaged distribution of the particle hydrodynamic diameters (H_D) based on their Brownian motion. To obtain reliable information on DNA sequences alone, the concentrations must be quite high; for example, Bombelli reported utilizing 3 μM concentrations to analyze a ~300 bp DNA sample that could form either linear or circular structures.[30] Moreover, when the size of the particulate materials becomes smaller than ~10 nm, the interpretation of DLS data becomes challenging because of an acute sensitivity to even a small admixture of larger particles that arises from the method's intrinsic dependence on radius as R^6.

Given the small size and diluteness of our DNA, we employed an indirect DLS protocol in which we initially attached the template DNA to a 15 nm diameter AuNP. In effect, use of the large AuNP amplifies the signal and allows us to get reliable data from significantly less material (~1.5 nM of AuNP). As described in more detail in the Methods section, thiolated-template ssDNA was mixed with citrate-stabilized AuNPs at reaction ratios of 50- (low density) and 200-fold excess DNA (high density) per AuNP, purified, and then hybridized with different combinations of complementary sequences before undergoing DLS analysis. Figure 5 shows a schematic of these DNA–AuNP assemblies along with representative data. Given that 15 nm AuNPs are predicted to display >600 dithiolate ligands on their surface[31] and have been measured to accommodate >100 thiolated DNA,[32] we expected high densities of DNA to be attached. To verify this, we measured the UV–vis absorbance of the DNA–AuNPs postconjugation following filtration using 100k MW cutoff microcentrifuge filters (data not shown). The results suggested average ratios of 20 and 60 DNAs per AuNP for the two reaction conditions of AuNP:DNA = 1:50 and 1:200, respectively, and these samples are hereafter referred to by these ligation ratios. Considering the number (N) of conjugated DNA on the surface of the template-labeled particle (AuNP-Temp), we can define the DNA footprint to be the average area that each DNA occupies on a given NP surface:[32]

$$\text{footprint of DNA} = \frac{4\pi r_{Au}{}^2}{N} \qquad (1)$$

where r_{Au} is the AuNP radius. Using this approach, the footprint for the 100 bp ssDNA was estimated at 11.8 and 35.3 nm^2 for the 60 and 20 ratio samples, respectively. These are far larger than the 6.0 nm^2 previously reported for 25 bp oligonucleotides chemisorbed onto the surface of the same-sized AuNPs.[32] More importantly, this confirms that our AuNP-Temp samples are far less densely packed and should thus have sufficient interoligo spacing for further hybridization reactions.

We report the DLS results as the average peak value of the intensity profile (in percent) for samples analyzed at five different scattering angles (see Table 2). The width of the intensity profile is also given as a gauge of the sample's polydispersity. The citrate-stabilized AuNPs are spherical in shape and have a core "hard" diameter of 15 nm with very little relative polydispersity. The H_D measured for these "as provided" NPs was, as expected, somewhat larger, with a diameter of 21.1 nm. This difference originates in the complexities of the hydrodynamic radius, which depends on the size/shape of the NP itself, on the chemical nature of the surface coating, and on the solvation layer.[33] Following conjugation with the 100 bp thiolated ss-template, the measured H_D of the AuNP-Temp construct more than doubled to 46 and 49 nm for the low- and high-density samples, respectively. The next set of samples consisted of both AuNP-Temp samples hybridized with the A, B, or C complements. For the low-density reaction, the H_D further increased by about

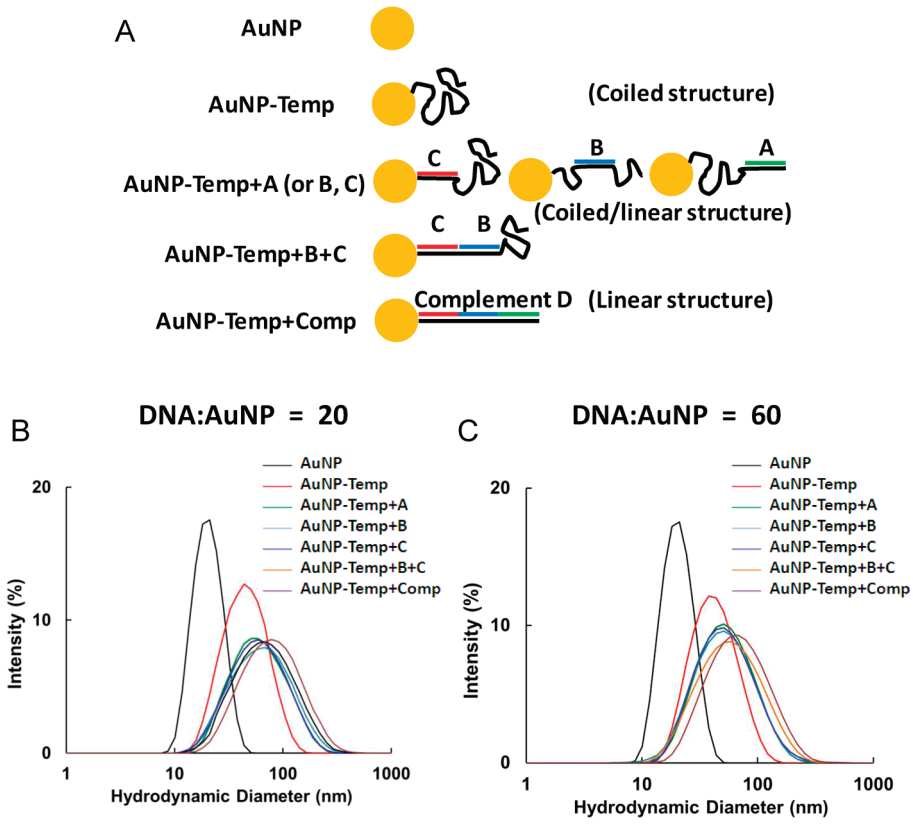

Figure 5. DLS analysis of 15 nm AuNP–DNA bioconjugates. (A) Schematic of the different AuNP sample configurations analyzed. Intensity profile data collected from AuNP:template DNA low-density samples, ratio ~20 (B) and high density samples, ratio ~60 (C) hybridized with the indicated complementary sequences.

TABLE 2. Hydrodynamic Size (nm) of Selected Gold Nanoparticle–DNA Conjugates

NP/reaction ratio	sample	hydrodynamic diameter, H_D[a]	estimated increase in radius[b]	increase in radius by DLS	increase in radius by hybridization[c]
AuNP [2 nM]	AuNP	21.1 ± 0.6 (6.5)			
DNA:AuNP = 20	AuNP-Temp	45.8 ± 0.9 (21.1)	14.2	12.4	
	AuNP-Temp + A	60.3 ± 2.5 (34.5)	22.7	19.6	7.3
	AuNP-Temp + B	60.1 ± 2.7 (38.5)	26.9	19.5	7.2
	AuNP-Temp + C	61.3 ± 2.3 (39.0)	22.7	20.1	7.8
	AuNP-Temp + B + C	68.1 ± 2.7 (43.3)	30.4	23.5	11.2
	AuNP-Temp + Comp	78.8 ± 2.5 (48.5)	34.0	28.9	16.5
DNA:AuNP = 60	AuNP-Temp	49.2 ± 1.3 (23.0)	14.2	14.1	
	AuNP-Temp + A	68.3 ± 2.5 (39.8)	22.7	23.6	9.6
	AuNP-Temp + B	74.0 ± 1.5 (47.1)	26.9	26.5	12.4
	AuNP-Temp + C	68.8 ± 3.4 (41.1)	22.7	23.9	9.8
	AuNP-Temp + B + C	79.6 ± 2.4 (50.6)	30.4	29.3	15.2
	AuNP-Temp + Comp	92.0 ± 4.5 (58.4)	34.0	35.5	21.4

[a] Average peak value of the percent intensity profile, $n = 5$ (at different angles) ± standard deviation. Numbers in parentheses: Width of the percent intensity profile. [b] Increase in radius estimated using the WLC model (eq 2) in conjunction with the 0.34 nm/bp length of dsDNA. [c] Derived after hybridization for each reaction condition.

15 nm in all cases to an average of 60.6 ± 0.6 nm, while the high-density reaction size increased by about 21 nm to an average of 70.4 ± 3.2 nm. The DNA structure for these three samples consists of a rigid ds-section that is adjacent to, or surrounded by, coiled ss-segments. Despite the differences in placement of the ds- *versus* ss-segments relative to each other, the increased H_D values are remarkably close within each AuNP sample. This implies that changes in the ensemble H_D alone cannot be used to determine the order and/or position of the hybridized segment in this format.

For the next analyses, both AuNP samples were jointly hybridized with complements B and C or the full 100 bp complement D. For the low-density sample, the H_D increased by ~7.5 and ~18 nm (compared to the

previous average), while the high-density sample grew by ~9 and 21.5 nm, respectively. Clearly, as the structure of the surrounding DNA becomes increasingly double-stranded and linear (and presumably extending further outward from the AuNP surface), the changes in DNA rigidity are directly reflected in the measured H_D; see also Table 2. In comparison to the H_D size of 21.1 nm for the AuNPs alone, the fully hybridized structures have increased in size by roughly 58 and 71 nm, respectively. These increases are consistent with the expectation based on each DNA duplex being about 34 nm, which suggests a diameter increase of twice that value, or 68 nm in H_D. Furthermore, it is not surprising that the increased occupation volume of the high-density sample should produce a slightly larger H_D.

Interestingly, these DLS results can allow us to infer additional information about the DNA and how it occupies the AuNP surface by applying a somewhat different analysis. From our data, the hydrodynamic radius of 100 bp of ssDNA is estimated at ~7 nm as *attached* to the AuNP, and this stands in comparison to values of 7.5 nm for 280 bps and 8.8 nm for 407 bps of *unattached* freely diffusing ssDNA.[34] On the basis of the H_D increases, we can estimate the hydrodynamic volume of the ssDNA on the surface of AuNP. In the case of the high-density sample (DNA:AuNP = 60), if we assume that the nonhybridized template DNA is essentially spherical from coiling and the H_D increases 28.1 nm from bare AuNP to AuNP-Temp, then we can also estimate the hydrodynamic volume occupied by the 100 bp DNA as 1452 nm^3 and the unit hydrodynamic volume of one base pair as 14.5 nm^3/bp. Using this estimate in conjunction with the length of dsDNA as 3.4 Å/bp, we can also estimate an increase in radius following hybridization with complements A, B, or C to be in the 23.5−31.0 nm range, which is consistent with the measured range of 23.6−26.5 nm. If the ssDNA is assumed to be in a random coil configuration on the NP, we can apply an alternate treatment to estimate the size of the ssDNA by solving the mean square end-to-end distance of a polymer $\langle R^2 \rangle$ using a worm-like chain (WLC) model:[35,36]

$$\langle R^2 \rangle = 2R_{max}l_p - 2{l_p}^2\left(1 - \exp\left(-\frac{R_{max}}{l_p}\right)\right) \quad (2)$$

Here $R_{max} = Mb$ is the maximum end-to-end distance of the actual polymer or the length of a fully extended ssDNA (where M is the number of base pairs and b is the 0.43 nm monomer size of ssDNA; see also schematic in Supporting Figure S3). l_p is the persistence length (stiffness) of the ssDNA, which is estimated at 2.5 nm in the 0.2 × PBS solution utilized for the DLS measurements here.[34] From this, the increases in radii were estimated and are shown in Table 2. Significantly, these values show a remarkable concordance with those measured from the high-density sample. For example, the estimated size of the 100 bp ssDNA in this sample was ~14.2 nm as compared to a predicted increase of 14.1 nm following DNA template conjugation. Using eq 2 in conjunction with a length of 3.4 Å/bp for dsDNA, we can also estimate an increase in radius for this same AuNP−DNA following hybridization with complement A, B, or C to be in the 22.7 (A, C) to 26.9 (B) nm range, which is again quite consistent with the measured range of 23.6−26.5 nm. Similar comparisons can be made for hybridization with B+C jointly (estimated 30.4 nm *versus* 29.3 nm measured) and full complement D (estimated 34.0 nm *versus* 35.5 nm measured). In the case of the low-density conjugation sample, the measured values were smaller than the calculated values, which we attribute to the lower density of ssDNA on the AuNP surface. This will allow for more flexibility in DNA configuration and a smaller radial contribution of the dsDNAs to H_D. This variability also suggests that it may be important to test several conjugation ratios when attempting this analysis. Nevertheless, these results allow us to again confirm hybridization and the presence of one-, two-, or full-complementary sequences on the template while attached to the AuNP.

FRET Spectroscopy. Because the FRET signal varies inversely as the sixth power of the separation distance between the donor and acceptor chromophores, it provides a powerful approach for measuring nanoscale distances in solution, including in cases where DNA is involved.[1,6−8,19,21,37−39] Although the range of FRET can extend up to 10 nm, the separation distances that can actually be measured depend directly on the photophysical properties of the selected donor and acceptor. Since the Förster distance, or R_0 value (*i.e.*, distance at which 50% energy transfer takes place; see Materials and Methods), for most dye pairs is 4 to 6 nm, and is specifically 5.5 nm for the initial 6-FAM/TAMRA donor−acceptor pair used here, measuring the intervals between our 11 nm complementary oligos is beyond the typical limit of single-donor/single-acceptor dye-based FRET system (>2R_0). One approach we used to address this problem is with internal labels, in particular measuring intermediate distances from a donor FAM at the 5′-terminus of the backbone strand to TAMRA labels placed at base 14 (4.8 nm) and base 23 (7.6 nm) of complement C, positions TAM1 and TAM2, respectively. A schematic giving the layout of these dyes appears in Figure 6A, with their spectral overlap shown in Figure 6B. It is important to note that when the dyes are positioned on the same side of the helix, the 0.7 nm dye linker lengths can allow some freedom of rotation toward or away from each other. However, if the dyes are rotated with respect to one another along the helix, as is the case with the TAM2 dye position, then the flexibility of the linker may have a much greater impact on the measured distance.[21]

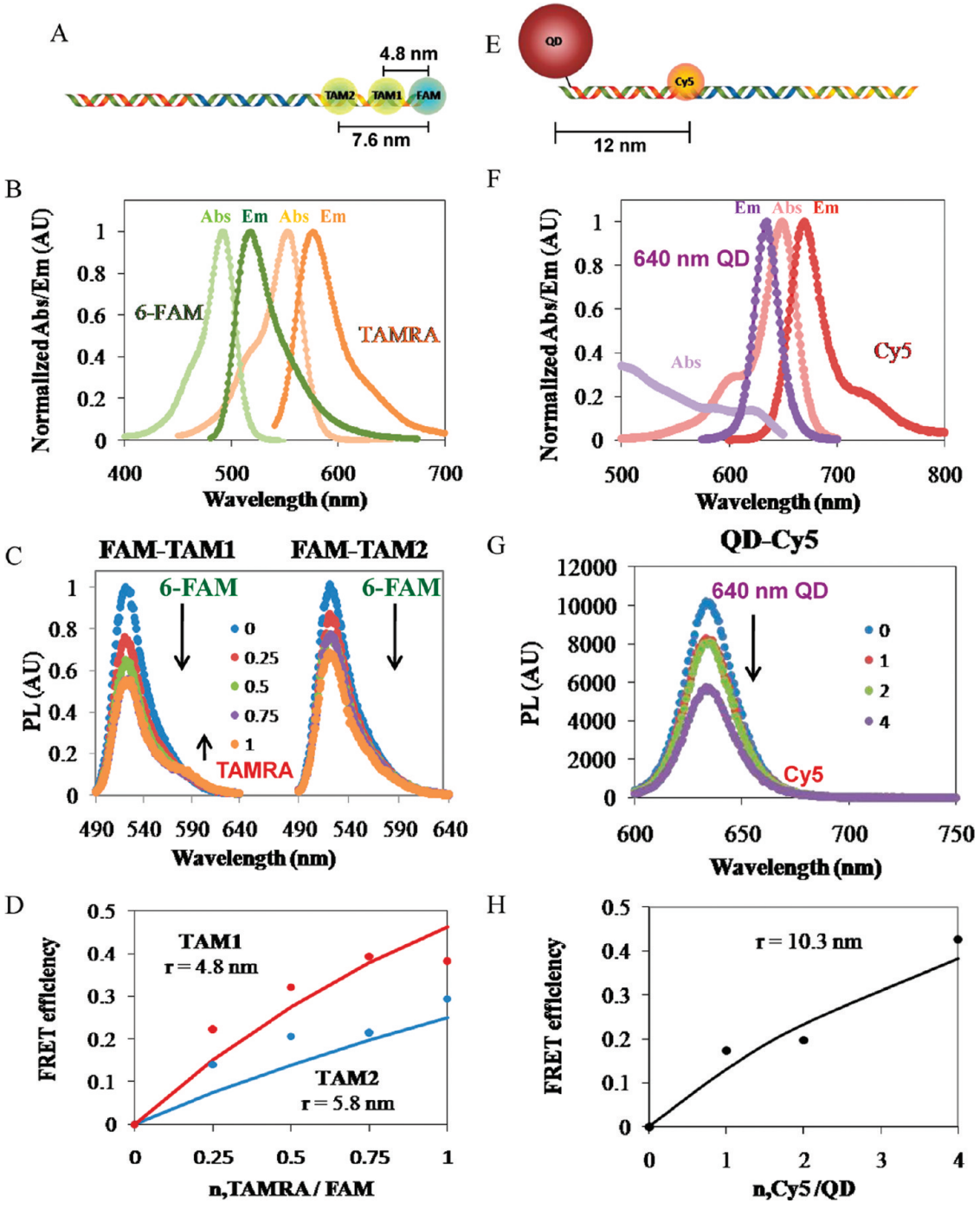

Figure 6. Fluorophore-functionalized DNA, QDs, and FRET. (A, E) Schematic of the nanoconstructs comprised of the FAM-labeled template or backbone DNA with one of two internally labeled TAMRA dyes positioned on the complement and a 640 nm emitting QD ligated to the A complement with the acceptor Cy5 attached to the 5′-end of the B complement. (B, F) Spectral overlap of the fluorophores used for each of the FRET experiments. (C, G) PL spectra with the direct excitation component subtracted. The FAM/TAMRA DNA structures were assembled in increasing fractional ratios of donor to acceptor from 0 to 1 and the QD/Cy5 structures with ratios shown at 0, 1, 2, and 4. (D, H) FRET efficiency *E* for each acceptor position *versus* acceptor valence derived from the data is plotted as points, while FRET *E* corrected for heterogeneity calculated using eq 4 is represented by the fitted line and indicates minimal deviation from assembly expectations.

FRET spectra were measured as a function of the acceptor−donor ratio in the range from 0 to 1 in monotonic steps of 0.25. As hybridization ratios can reach only a maximum of 1:1, the partial ratios serve to provide a better incremental estimate of overall FRET efficiency. In processing the data, the direct excitation of the acceptor as collected from control samples was subtracted from the primary spectra, and the difference spectrum for each dye position is then plotted (see Figure 6C). Lastly, the calculated efficiency plotted as a function of the donor-to-acceptor ratio is fit to determine the distance using eqs 3−6 (see Materials

and Methods), and the results are summarized in Figure 6D. The TAM1 acceptor position relative to the donor obtained in this way was 4.8 nm, which is the expected value. In contrast, the TAM2 acceptor position was found to be 5.8 nm, which is 1.8 nm (~24%) less than expected. A small amount of FRET sensitization of the TAMRA acceptor is seen in the closer TAM1 configuration as expected. This becomes negligible for FRET to TAM2. A low rate of TAMRA dye sensitization correlates with previous reports, and indeed this has led to it being sometimes used in the role of a generalized quencher.[37] We attribute the difference between expected and derived separation distances for TAM2 to stem from a combination of factors including the acceptor position on the DNA, the linker length (which can allow rotation either toward or away from the donor), and the limitations of the TAMRA dye as an acceptor when placed at this extended separation distance.

A second and more directly comparable approach to using FRET for characterizing our DNA construct is to introduce a semiconductor quantum dot into the system, as shown in Figure 6E. When a 640 nm QD donor is paired with a Cy5 dye acceptor, R_0 increases to about 7.5 nm as a direct consequence of Cy5's large extinction coefficient (250 000 M^{-1} cm^{-1}) combined with the QD's strong quantum yield of ~40%; this value is now large enough to probe the full distance of one segment along the DNA backbone (~11 nm). To attach the QD to the DNA, an amine-labeled DNA is attached to a HYNIC-terminated peptide using hydrazone linkage chemistry (see the Methods section). The other end of the peptide displays a His_6-motif, which readily self-assembles to the QD surface with all six histidines believed to be in direct contact with the QD surface and thus contributing negligible lateral extension.[38] The peptide linkage in this case is estimated to add ~2–3 nm to the total length between the QD and the Cy5 dye.[1] The FRET measurements were taken in much the same way as earlier, except that a wider range of acceptor–donor ratios is accessed. Because the QD attachment is a self-assembly process, the initial stoichiometry will affect the average number of DNA strands that attach to each QD. In our experiment, the QD (donor) concentration was held constant while the DNA (acceptor) displayed around it was increased incrementally from 0 to 4× that of the QD concentration. This format allows access to the unique FRET properties available to QD donors. In particular, since the QD has a nontrivial surface area, multiple acceptor moieties can be arrayed around each central nanocrystalline donor, and this will increase both the acceptor absorption cross section and the FRET probability. As this single-donor/multiple-acceptor configuration can allow for efficient FRET processes to be realized over relatively longer distances (see ref 39 for a detailed description), it allows us to probe the much longer donor–acceptor separation distance present despite

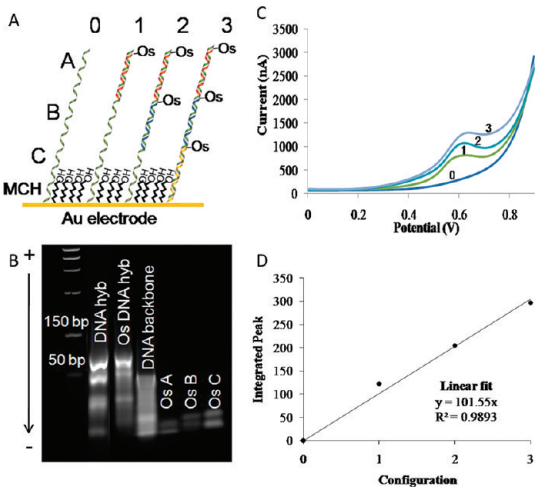

Figure 7. Osmium-functionalized DNA and electrochemistry. (A) Schematic of the sample format for the electrochemistry experiments. (B) 1% agarose gel showing the comparative migration of an Os-labeled and unlabeled hybridized DNA construct. (C) Current–voltage curve of the square-wave voltammetry showing the signal increase at 0.6 V with each complement addition. (D) Plot of the linear relationship between the integrated area under the peak and number of osmium atoms assumed to be hybridized to the DNA backbone in each configuration.

the extra lengths contributed by the QD and its peptide linker.[39] The composite PL spectra obtained are shown in Figure 6G, and we again note a low level of Cy5 acceptor sensitization in this configuration, which also correlates with previous reports.[40] The resulting FRET efficiency is plotted in Figure 6H, and calculations using eqs 3–6 yield a separation distance of 10.3 ± 0.1 nm as compared to the expected 12.2 nm.

The discrepancy between the expected and measured QD–dye distances can have several origins. While the DNA itself should be linear and rigid in solution, there is some freedom of motion in ligands attaching the QD and dye, which can allow them to move toward or away from each other. In addition, the DNA bases located near the chromophores can increase or decrease the FRET efficiency.[41] Previous experiments using a structurally similar architecture and attachment chemistry combined with modeling indicated that a nonperpendicular attachment to the QD can produce a nanostructure with FRET distances that are smaller than expected.[1]

Electrochemistry. Voltammetry techniques can be used to detect/confirm the hybridization of complementary oligos to the backbone DNA by introducing an appropriate oxidizer. For our work, we use a reactive osmium isothiocyanate (OsICN) molecule chosen for its known oxidation potential and for its facile site-specific covalent attachment to the DNA *via* an amine linker. To confirm proper assembly prior to the electrochemical measurement, a 1% agarose gel was run with the template hybridized to all three Os-labeled complements, and as a control, the template hybridized

with three unlabeled complements. The gel image in Figure 7B confirms formation of the full structure and reveals a slight migration difference between unlabeled and Os-labeled DNA structures, with the OsICN probe apparently acting as an electrophoretic "parachute" and slowing the DNA .

In setting up the voltammetry experiment (schematic in Figure 7A), the template was utilized with a thiol on the 5′-end so that it would self-assemble or chemisorb onto a gold electrode. The electrode was then backfilled with mercaptohexanol to prevent nonspecific adsorption. Hybridization proceeded one complement at a time starting farthest away from the electrode and moving inward. Each Os-labeled oligo was given 2 h to hybridize to the substrate-attached backbone at room temperature. The measurement was then taken in a phosphate buffer containing Tween 20. This detergent was added to the buffer in order to ensure that nonhybridized DNA did not absorb to the surface and also to prevent reaction of the buffer at the electrode surface. Measurements were collected by scanning between 0 and 0.8 V to cover the Os-oxidation peak at 0.62 V. Figure 7C shows the sequential increase of the peak height as each DNA sequence is added. Integrating each peak (with the background subtracted) yields an estimate of the quantity of Os absorbed to the electrode. When these integrated values are plotted (Figure 7D), we observe a strongly linear trend with the least-squares best-fit shown. This suggests the voltammetry is providing a semiquantitative direct measure of the attachment of the Os-labeled DNA in a somewhat close to a real-time format. These results also confirm, at least for this DNA structure, that the order of DNA hybridization is not critical since the area closest to the electrode was hybridized last without compromising either the detection capability or the assembly process itself.

DISCUSSION AND CONCLUSIONS

The successful development of DNA nanostructures as useful platforms within nanobiotechnology is critically dependent on the available means for characterizing, monitoring, and controlling their behavior. In this report, we use a simplified test-bed consisting of a 100 bp duplex DNA sequence displaying various site-specific molecular and NP functionalizations, to which we apply seven different characterization methods. The two most commonly used in the literature are gel electrophoresis and AFM, and to this basic set we have added voltammetry, DLS, TEM, FRET, and structural modeling. We recognize that many of these techniques have been previously applied to analyzing DNA structures; however, to the best of our knowledge, this number and variety of analytical techniques have never been applied in concert to analyzing a single DNA-organized structure. The questions we attempt to answer from this analysis reflect the important basics of all such DNA constructs, namely, was the hybridization successful and correct, can we measure the spacing between any two (or more) given points within the structure, and with what fidelity was the desired geometric structure obtained? In the following we consider each of the seven techniques in turn, highlighting the advantages and disadvantages of each. In addition, we look to bring out the synergistic information obtainable when the results of the various methods are combined for a multimodal characterization.

As an important first step prior to the physical characterization, we began with structural modeling to determine how the DNA modifications or probe/dye labeling would affect the overall structure. In particular, we were interested in how much mass, additional length, and rotational flexibility each modification would contribute. Adding to the impetus driving our study, we find that all direct modifications made to the DNA, including the OsICN, dyes, and linkers, contribute very little mass to the composite structure (<3%). Similarly, the structural modeling also indicates that these same modifications contribute less than 10% to the gross length of any final composite assembly with the exception of the His_6-peptide-HYNIC, which increases the size by ∼15% when present at the terminus. By contrast, the 15 nm AuNP and QD sizes approach that of the dsDNA structure, which indicates that their large size must be carefully considered in any analytical implementation. In practice, these larger NP materials were used here in a role analogous to a central nanoscaffold surrounded by the DNA, and the persistence length of the DNA in different hybridized configurations was then probed with either FRET or DLS. The FRET analysis accounted for the QD size contribution, while the DLS analysis relied on the AuNP to "amplify" the signal as discussed below. This approach is thus necessarily somewhat converse to the other analytical formats in that it places multiple DNAs around a single copy of each (large) particle, rather than multiple (small) probes on a single DNA. Overall, the modeling provided an initial understanding of the labeled-DNA structures, along with a quantitative basis for understanding the dimensional constraints imposed by the various modifications and probes within each analytical format.

For initial characterization of a variety of DNA structures ranging from PCR products to origami, the standard tool remains gel electrophoresis. The measurement is quick and routine, being useful, for example, for confirming that hybridization has indeed occurred or for estimating labeling efficiency. The measurement can work with either labeled or unlabeled DNA, and in addition to yielding characterization data, it can also be used for isolation and purification.[19] However, the structural information it provides is quite limited and indirect, being lumped into the

single composite quantity of electrophoretic mobility. Furthermore, electrophoresis tends to require more material than the other techniques considered in this paper, and this is often a serious consideration in DNA-based assembly, where nanomolar quantities are common. As a second method for initial characterization following hybridization, we employed square-wave voltammetry. This electrochemical technique is likewise relatively simple, but it has the further advantage of needing far less material. For example, we estimate that around 0.2 pmol of backbone DNA was assembled onto the electrode surface during the experiments described above, while in contrast, we commonly loaded at least 20 pmol of DNA per lane for the agarose gel electrophoresis. Another potential advantage of an electrochemical approach is its temporal resolution, which is far higher than gel electrophoresis, and this can be used to provide near-real-time information, such as confirmation of stepwise hybridization (as we have discussed) or even some kinetic information. Like electrophoresis, the structural information derived from voltammetry is indirect and necessitates interpretation, a process that is often complicated by the need for a much deeper understanding of the underlying electrical processes.

The DLS analysis provides data that complements that collected from electrophoresis and the electrochemistry. The increasing diameters measured confirm attachment of the ss-template to the AuNP and then follow the selective hybridizations of multiple sequential complements. As applied here, the DLS analysis comes with two intrinsic benefits. First, utilizing the AuNP as a central nanoscaffold serves as an amplifier of the DLS signal while simultaneously avoiding the limitations of DLS for small sizes (<10 nm). This allows us to use significantly less sample than previous DNA-only analyses of similarly sized constructs, *e.g.*, 1.5 nM AuNP *versus* 3 μM.[30] Despite the average of 20 or 60 DNAs attached to each AuNP, this still represents 2 to 3 orders of magnitude less sample. Second, this approach simplifies the subsequent analysis since we treat the surface DNA as essentially a NP-surface ligand in which intrinsic rigidity is introduced by hybridization. The measured increases in size during hybridization correlate extremely well with predictions, and we find that DLS analysis further provides interesting and useful information about the overall bioconjugate beyond just DNA length. For example, the data allow us to extrapolate the DNA's volume along with the footprint and volume that it occupies on the AuNP surface in selected configurations.

More direct structural information is provided by AFM, and for this reason AFM is generally the primary tool used for detailed characterization of functionalized DNA structures (except in the rare case of true 3-D structures).[19,42] AFM requires that the structure be situated on a surface, and it can be done either in air or in an aqueous environment, with the latter often preferred for DNA imaging. Also, since having high spatial resolution is usually important for DNA structures, it is essential that one use ultrasharp probe tips. For imaging DNA itself, AFM combines adequate resolution with relative ease and low cost. For imaging composite structures, AFM is attractive due to its sensitivity to topography, which allows the observation of attached components such as AuNPs. In general, our AFM experience and results bear out these statements, although we find that the resolution and repeatability seen in the AFM are not as good as with TEM or FRET. This is partly due to tip convolution effects, but the AFM resolution is likely also compromised by imperfect surface adhesion and consequent movement of the sample by the tip. We suspect that these effects are amplified by the small size of our structures, and it may be that their attached particles also increase the likelihood of undesired motion. Indeed, we found that with conventional aqueous AFM it was impossible to produce clear images of distinct structures (data not shown) and that only under dry conditions was AFM characterization of our model structures successful. The measured average particle spacing of 11.3 $\pm$ 1.9 nm corresponds closely to the 11.2 nm expected for our construct when in the B-DNA form, suggesting that our "dry" DNA is remaining essentially hydrated. It is plausible that surface interactions as discussed by Feng are also acting to stabilize the B-DNA structure.[20]

TEM is, of course, a common imaging technique that is known equally for its high resolution and its often-difficult sample preparation. With some exceptions, it is generally not used for imaging nanostructures composed solely of DNA because of the lack of atomic contrast and the challenge of distinguishing the carbonaceous biopolymer from the underlying ~10 nm thick holey carbon support. As presented here, one can improve the contrast by attaching metallic NPs, whose high contrast and discrete particle spacing make size characterization with TEM quite effective, including minimizing any confusion associated with inadvertent contamination. Our TEM measurements estimate the average interparticle spacing to be 10.0 $\pm$ 1.0 nm instead of the 11.3 nm obtained from AFM. We believe the difference results mainly from the fact that the TEM is performed under high-vacuum conditions, which causes considerable drying of the DNA component and perhaps even converts it from the hydrated B form to the wider, shorter A form. Some evidence for at least a partial conversion is the observation that the TEM-measured distance is intermediate between the expected values of 8.6 nm for A-DNA and 11.2 nm for B-DNA. Clearly, if the intended use of a DNA-based assembly is in a thoroughly dried condition, then TEM characterization would be favored over conventional AFM. More intriguing, however, is the idea that

multimodal characterization using AFM and TEM can allow for a rough assessment of the degree to which hydration determines the relative positioning of components when DNA is used as the underlying assembly methodology. It is also important to point out that the TEM analysis was the most challenging for several reasons. Despite the AuNP contrast, the high background made it hard to discern individual particles from background or even two joined AuNPs. The images had to be processed as described in the Methods and then carefully analyzed. Only the presence of three contiguous linearly arranged AuNPs with the roughly expected distance separating them could be confidently identified. This also made it hard to estimate the number of partially labeled assemblies, as was done for the AFM analysis, although we expected a similar distribution given that the samples were prepared in the same manner.

The AFM and TEM methods are more or less directly comparable, since both evaluate DNA–NP composites situated on surfaces under "dry" conditions. In contrast, FRET characterization as applied here uses spectroscopic methods to examine DNA–chromophore composites residing in an aqueous environment with no solid substrate. This can be advantageous because the needed equipment and analysis are far simpler than those used for the imaging methods. In addition, for many applications (*e.g.*, in biosensing), this measurement condition is much closer to that of actual use. Finally, of great interest to us is the fact that FRET offers a *different* perspective on the same structure, with information that is complementary if not "orthogonal". An important consideration for attempting this analysis is to make sure that the donor–acceptor Förster distance is sufficient to reliably measure the structures or point-to-point distances in question. Interestingly, some recent publications have shown that pairing long-lifetime Tb-chelate-donors with QDs acting as FRET acceptors allows access to quite large R_0 values of >10 nm, which would allow for the extremely long FRET distance measurements in structures such as this.[43] Moreover, the same format can also allow for multiple simultaneous or "multiplexed" distance measurements, which would be particularly helpful with complex structures such as DNA origami.[44,45]

As presented above, the most relevant FRET comparison occurs when the donor–acceptor pair is a QD donor surrounded by multiple dye/analytes since this provides an interaction distance that is well matched to the repeat distance of the DNA composite considered in the AFM/TEM studies, namely, 11.3 nm. The FRET measurement found the distance to be 10.3 nm, or about 1 nm smaller. Overall, this demonstrates quite good agreement among all three quantitative measurements. Furthermore, the ~10% discrepancy between the FRET and the AFM/TEM findings may well be informative. To explain this, we note that the FRET signal represents an ensemble average that, because the FRET efficiency varies as $1/r^6$, will be dominated by the chromophores that happen, as a result of thermal motion, to be situated most closely together at the time of the measurement. Thus, absent other perturbations, FRET's "spectroscopic ruler" provides essentially a measure of the chromophores' distance of *closest* approach within the ensemble rather than their *average* distance. The difference between these distances is set by the chromophores' range of motion, and this is mostly determined by the flexibility of the attachment ligands. The dye attachments are relatively short, with an amine linker equal to a length of less than 1.0 nm, but the QD donor's peptide linker is longer, being 2–3 nm in addition to the amine linker, and when combined this contributes significantly to increased freedom of movement. Furthermore, as simulated in the work of Boeneman *et al.*,[1] additional flexibility enters as a result of the DNA being tilted with respect to the QD surface. Finally, the fact that the DNA–chromophore composite is not constrained to lie on a supporting surface and can thereby "flex" is, we believe, a much less important contributor to variation in the interchromophore distance given the stiffness of the DNA duplex.

As a result of these considerations, we conclude that by combining the FRET measurements with AFM characterization (which, as noted earlier, appears to measure the B-form of DNA even when the measurement is performed in air under nominally "dry" conditions), one can obtain new information on the actual range of motion of the attached components. In our case, the difference between the measurements of 1 nm indicates that the actual positions of the components (and particularly of the less-constrained QD) varies by about 2×1 nm = 2 nm. It should be noted that this is somewhat less than that expected from the theoretical arguments, a difference that presumably results from steric limitations. Recast in practical terms, what the multimodal characterization results are saying is that if in a particular application (*e.g.*, a biosensor) we are using DNA methods to precisely position QDs, then the actual uncertainty in the QD position using the His_6-peptide attachment chemistry would be about 2 nm. This uncertainty could also be significantly decreased by using smaller and more structurally constrained linkers.

In summary, we have utilized a model 100 bp multifunctionalized DNA system to examine a variety of techniques for characterizing DNA structures. To compare and contrast among these methods and to appreciate the possible benefits of multimodal characterization, we studied different versions of the same DNA structure displaying various NP or molecular labels with multiple methodologies. Despite modifying the DNA structure with a number of different molecules and probes that range from small dyes to AuNPs approaching almost half the DNA length in size,

useful information can be obtained in each case, and we are still able to readily confirm formation and/or evaluate the underlying structure. In general, the data suggest that the modifications and probes, in and of themselves, do not significantly perturb the underlying DNA structure. As we have seen, depending upon what is ultimately required to understand and characterize a particular DNA structure (which often depends not just on the DNA but also on its environment), each method can contribute differing amounts of information and insight. Moreover, each method has its advantages and disadvantages, with some being directly sensitive to DNA, whereas others require labels to improve contrast or provide signal. The simplest parameters that were repeatedly confirmed were dimensional ones associated with various point-to-point separations along with verifying hybridization. In contrast, the exact order of DNA assembly during hybridization can be quite challenging to confirm, at least with the techniques applied here. The gross linear structure of the DNA was repeatedly confirmed by modeling, TEM, AFM, DLS, and FRET. These techniques also provide the most quantitative spatial information, and in our case, all are in good agreement as to the actual distances, *i.e.*, within roughly 1 nm. Moreover, when combined with an understanding of the DNA structure and the linkage chemistry, one can develop an understanding of the source of origin of the small differences between the measured distances. In particular, we found that such multimodal characterizations could assess the degree of dehydration of the DNA sample and could probe the degree of flexibility of the linkage chemistries. Overall, these results suggest that multiple analytical modalities can be applied to more complex DNA structures such as origami and be effectively used to confirm hybridization, overall size, or MW, along with making point-to-point distance determinations. In this way, the use of multiple characterization methods can provide both corroboration and a greater understanding of the underlying dynamic nature of such nanostructured DNA architectures.

MATERIALS AND METHODS

DNA Sequences. The DNA used in these experiments consisted of a *de novo* synthetic 100 base-pair single-stranded DNA backbone with the following sequence: 5′-CTAGACGA AACTGTATGAATTGCATCGATCTTCTGATACATAGCTATTACATCGAATTA TGTTCTATGTCGCCAACTCTGAGTCGTAACCGCGATAGC-3′. The complementary sequence was divided into three sequential segments designated A, 5′-GCTATCGCGGTTACGACTC AGAGT TGGCGACAT-3′; B, 5′-AGAACATAATGTTCGATGTAATAGCTATG-TATCA-3′; and C, 5-GAAGATCGATGCAATTCATACAGTTTCGTC-TAG-3, and these correspond to sizes of 33, 34, and 33 bases, respectively. A contiguous 100 bp sequence that was directly complementary to the above backbone was also obtained and is designated D. DNA was obtained from Operon Biotechnologies, Inc. (Huntsville, AL, USA). Following synthesis, the DNA was HPLC purified and the sequence confirmed by mass spectral analysis where appropriate. To allow for a variety of covalent attachments, the DNA was purchased both unlabeled and with chemical or fluorescent modifiers inserted during synthesis. As shown in Figure 1, the backbone was modified on the 5′-end with an amino C6 (primary amine on a 6-carbon alkane linker), thio S−S (protected disulfide), or carboxyfluorescein (FAM) fluorescent dye. The A, B, and C complementary segments were obtained modified on the 5′-end with an amino C6. The middle 34-base B segment was also obtained with a Cy5 label on the 5′-end, and the 33-base C segment was purchased with tetramethylrhodamine dye (TAMRA) labeled on the 5′-end or alternately placed in the C2 and C3 positions located at the thymine residues 14 and 23 bases from the 3′-end, respectively; see Figure 1. Chemical structures for all the DNA modifications are shown in the Supporting Information.

Structural Modeling. The double-stranded DNA model was constructed using *make-na*, a web-based utility (http://structure.usc.edu/make-na/) that builds a 3-D model from a linear DNA sequence using Nucleic Acid Builder (http://casegroup.rutgers.edu/casegr-sh-2.2.html).[46] The model was built using the sequence of the *de novo* synthetic 100 bp ssDNA backbone given above along with another model of the 10 bp sequence at the 5′-end. The thickness of the phosphine-ligand layer on the AuNP was estimated to be 8.5 Å from a model of 4,4′,4″-phosphinetriyltris(*N*-methylbenzamide) constructed using ChemBioDraw and ChemBioDraw-3D (Cambridgesoft.com). The thickness of the DHLA was previously estimated to be 9−11 Å and is represented in these figures as a shell 10 Å larger than the QD.[47] All other models were created using tools in UCSF Chimera (version 1.4.1).[48] Energy minimization was carried out in Chimera using built-in features including ANTECHAMBER (version 1.27) and the AM1-BCC method of calculating charges.[49] After building the DNA−linker, DNA−fluorophore, and DNA−peptide models, the maximum area the fluorophore or end-group could occupy was estimated by producing an extended version of the peptide or linker and using that to define a radius from the attachment point on the DNA. These areas are represented by translucent shells in Figure 2A. Starting on the top line the shell for the thiol linker has a radius of 10.1 Å; the amine is 9.8 Å; and OsICN is 16.3 Å. In the center is the peptide linker (sequence HYNIC-Gly-Leu-Ala-Aib-Ala-Ala-Gly-Gly-His_6) containing a helical Ala-rich segment joining the HYNIC attachment to the DNA and the extended poly-His motif. This much larger structure has a scope of 53 Å. Across the bottom of the figure are Cy5 (16.5 Å), TAMRA (20.1 Å), and 6-FAM (19.8 Å). Comparative sizes of the various probe components used are shown in Figure 2B, which depicts (from top to bottom) a 1.4 nm AuNP with a 15.5 Å shell (to approximate the phosphine ligand and linker covering this particle), 6-FAM, a QD with a DHLA coating ~10 Å thick, a 15 nm AuNP, and on the right the 100 bp segment of DNA. As the thiolated DNA chemisorbs directly to the AuNP surface, the stabilizing citrate ligand present is not shown on its surface.

Gel Electrophoresis. DNA samples were mixed with 6× gel loading dye (New England Biolabs) and loaded into the indicated percentage agarose gels buffered with 1× TBE buffer (89 mM Tris-borate, 89 mM boric acid, 2 mM EDTA, pH 8.3) in 1× TBE running buffer and prestained with gel red intercalating dye (Biotium). Typical sample concentrations were 20 pmol of DNA in a volume of less than 25 μL. The gel was run at ~10 V cm^{-1} for 1 h at ambient temperature. The DNA bands were visualized on a Gel Logic 2200 imaging system (Carestream) equipped with a 535 ± 50 nm cutoff filter.

Gold Nanoparticle Conjugation for TEM and AFM Studies. DNA segments were functionalized with 1.4 nm AuNPs using monosulfo-NHS-Nanogold (Nanoprobes, Inc. Yaphank, NY, USA) following the manufacturer's instructions; see Figure 1. For this, the backbone DNA was hybridized with all three amine-labeled segments in 0.1× phosphate-buffered saline (PBS, 1× = 0.1 M sodium phosphate, 0.15 M NaCl, pH 7.4) using an Eppendorf

MasterGradient thermal cycler with the following program: 95 °C for 3 min followed by a ramp down of 1 °C per minute until 4 °C was reached. The Nanogold powder was hydrated in 18 MOhm deionized water and then directly added in 15 molar excess to the prehybridized DNA structure. The solution was left to react at room temperature for at least 2 h. Hybridization was confirmed by monitoring the migration shifts, relative to the individual segments, using gel electrophoresis. Excess unlabeled AuNP and improperly hybridized material were filtered using a Millipore Amicon Ultra 30,0000 NMWL centrifugal filter prior to analysis.

Osmium Isothiocyanate Ligation. For the electrochemical study, a reactive osmium isothiocyanate, $[Os(bpy)_2(phen\text{-}NCS)][PF_6]_2$ ($\varepsilon_{450} = 12\,500\ M^{-1}\ cm^{-1}$), was synthesized from $(NH_4)_2OsCl_6$ as described by Prasuhn.[50] Once the compound was synthesized and dried down, it was covalently coupled to the amine-labeled DNA segments; see Figure 1. For this, 10 nM aminated-DNA was added to 1 mg of Os isothiocyanate (OsICN) solubilized in 300 μL of dimethylsulfoxide (DMSO). A 300 μL volume of 0.136 M sodium tetraborate was added to bring the pH to 8.5, and the reaction was gently agitated overnight at 4 °C. The Os-labeled DNA was purified on a PD-10 column (GE Healthcare) in 50 mM triethylammonium acetate buffer. The concentration was determined using an Agilent Technologies 8453 UV−visible spectrophotometer, and the labeled DNA segments were dried down and stored desiccated at −20 °C before further use.

Quantum Dot−Peptide Conjugation. For the FRET studies, CdSe/ZnS core/shell semiconductor QDs with an emission maxima at ~640 nm were synthesized using a standard high-temperature reaction of organometallic precursors in hot coordinating solvents.[51] These QDs were made soluble in aqueous media through exchange of the native capping shell with dihydrolipoic acid (DHLA). The QD is attached to the 5′-end of segment A *via* a $(His)_6$ peptide coupled to the DNA's amine functional group. This ligation chemistry employs a 2-hydrazinonictinyol (HYNIC)-modified $(His)_6$-peptide and has been described elsewhere in detail;[52,53] see Figure 1C for peptide-conjugation chemistry. Briefly, the amine-labeled DNA, 0.5 mM, is first reacted with *p*-formylbenzoic acid-*N*-hydroxysuccinimide ester (9.09 mM, Sigma-Aldrich) in 1× PBS to form an aldehyde-modified DNA adduct. The reaction was carried out overnight at room temperature with slight agitation, purified using two consecutive PD-10 columns, and dried down using a SpeedVac. Peptide DNA ligate was produced through reaction of the HYNIC-modified $(His)_6$-peptide (1 mM in 10% DMSO/0.1 M ammonium acetate pH 5.5) with the formylbenzoic-modified DNA (2 mM) in the presence of aniline. The reaction proceeded overnight in the dark, and peptide−DNA conjugate was purified using Ni-NTA media (Qiagen, Valencia CA, USA), desalted on an oligonucleotide purification cartridge (Applied Biosystems, Forster City, CA, USA), and quantified *via* the hydrazone bond UV absorption ($\varepsilon_{354} = 29\,000\ M^{-1}\ cm^{-1}$). The DNA peptide conjugate was then dried down for storage as described in detail by Sapsford *et al.*[54]

Electrochemical Data Collection. For the electrochemical experiments, oligos A, B, and C, were ligated with the OsICN as described. After lyophilization, each DNA was resuspended at 2 μM in 0.1× PBS buffer supplemented with 0.05% Tween 20. As purchased, the thiolated backbone is provided as a protected disulfide, and so processing began with a deprotection step. For this, 20 nmol of the disulfide-terminated 100 base-pair backbone DNA was hydrated in 50 μL of DI water. A 5 μL amount of 1 M dithiothreitol was added to deprotect the disulfide bond at 37 °C overnight. The DNA was then purified on two PD-10 columns sequentially run with DI water and 10 mM Tris-Cl pH 7.5 and 1 mM EDTA (TE) buffer. The final product was diluted in 10 mM Tris-Cl, pH 7.5. EDTA (TE) buffer (1 mM) to a final concentration of 2 μM and supplemented with 2 M NaCl and 0.05% Tween 20. Electrochemical measurements were taken using a 1.6 mm gold disk stationary voltammetry working electrode, a Pt wire counter electrode, and an Ag/AgCl reference electrode (BASi, West Lafayette, IN, USA). The gold electrode was placed into the DNA solution overnight to allow for self-assembly. After the template DNA self-assembled to the electrode, but before any further hybridization with the Os-labeled oligos, the electrode was submerged into a 1 mM solution of mercaptohexanol to allow backfilling for 1 h as per Herne and Tarlov, which helps to prevent any nonspecific binding to the electrode.[55] Hybridization of each oligo was performed separately by placing the template-coated electrode into one of the Os-labeled oligo solutions, A, B, or C, for 2 h. Voltammetry was recorded before and after each hybridization step on a CHI 440 potentiostat, in 0.05% Tween 20 containing 0.1× PBS buffer, using a square-wave potential sweep. The potentiostat parameters were set to record from 0 to 0.9 V with a 0.004 V increment. The square-wave amplitude was 0.025 V at 15 Hz with a quiet time of 2 s and a sensitivity of 2×10^{-6} V.

TEM Image Collection. TEM samples were prepared by treating a 200 mesh holey amorphous carbon coated TEM grid with 10 μL of poly-L-lysine (0.5 μg/mL) for 1 min as per Williams.[25] The excess was wicked away, and the grid was rinsed twice with DI water and allowed to dry. Then 20 μL of gold-labeled DNA solution at 10 nM concentration was placed on the grid for 5 min to allow the DNA to adsorb on the surface. The excess liquid was wicked away, and the grid was rinsed once with DI water and allowed to dry. Images were taken using a Hitachi H9000URH HRTEM operating at 300 kV. Image processing was done using Image J software (NIH). To differentiate the AuNP from the background noise, the images were smoothed until the higher contrast particles could be clearly distinguished. The processed image was then compared to the original in order to determine where the particles existed in linear 3-point arrangements.

AFM Image Collection. For AFM sample preparation, freshly cleaved mica was prepared by treating with 40 μL of 2 mM NiCl solution for 5 min. The mica was rinsed in water and allowed to dry. A 20 μL sample of gold-labeled DNA solution was placed on the pretreated mica for 5 min and then rinsed in water. The excess was wicked away, and the sample was allowed to dry. AFM measurements were performed on a Veeco Multimode with the Nanoscope IIa controller (Veeco Instruments). Imaging was done using ultrasharp diamond-like carbon tips (MikroMasch). Images were analyzed using WSxM software[56] and IDL particle tracking software[57] to obtain pair correlation statistics.

Dynamic Light Scattering Analysis. *Conjugation of AuNPs to DNA: AuNP−DNA.* 5′-Thiol-modified single-stranded template DNA was conjugated to 15 nm diameter citrate-stabilized AuNPs obtained from Ted Pella Inc. (Redding, CA, USA). For this, 2 nM AuNPs were reacted with 100 nM or 400 nM DNA in 0.1× PBS, corresponding to a reaction ratio of DNA per AuNPs of 50 for the low-density and 200 for the high-density DNA conditions, yielding, respectively, estimated ratios of 20 and 60 DNA/AuNP. The mixtures were gently stirred at room temperature for 8 h. Then nonconjugated free DNA was removed by washing three times with 0.5× PBS, and the conjugates were purified using a centrifuge filter (Millipore, 100K MW cutoff). The two different AuNP−DNA samples were washed, concentrated to 20 nM, and kept at 4 °C for future use.

DNA Hybridization to AuNP−DNA Conjugates. Complementary sequences A (33 bp), B (34 bp), and C (33 bp) or the full complementary sequence (100 bp) was hybridized with the as-prepared AuNP−DNA. For this, 100 μL of stock AuNP−DNA (20 nM) was reacted with excess amounts of the complementary DNA's, 200 μL of 10 μM A, B, C, and D or B and C together, respectively, in 0.5× PBS. The DNA/AuNP−DNA mixtures were melted at 80 °C for 30 min, slowly cooled to 37 °C and kept at that temperature for 4 h, and then kept at room temperature until the DLS measurement, where they were diluted to 1.5 nM.

DLS. Measurements were performed on a CGS-3 goniometer system equipped with a HeNe laser illuminating at 633 nm and a single photon counting avalanche photodiode for signal detection (Malvern Instruments, Westborough, MA, USA). The autocorrelation function was performed by an ALV-5000/EPP photon correlator and analyzed using Dispersion Technology Software (DTS, Malvern Instruments). All the samples were prepared in water (0.2× PBS) and filtered through 0.2 μm syringe filters (Millipore). The sample temperature was maintained at 20 °C during measurement. The autocorrelation function was an average of three runs (10 s each) and then

repeated with at least five different scattering angles ranging from 80° to 130°. To extract the contributions from different size populations, we used the CONTIN algorithm (DTS software). The intensity profile was obtained by fitting the correlation function to a multiexponential using CONTIN. The intensity profile is more sensitive to small microscopic aggregation than volume or number profiles because the scattered intensity follows an R^6 dependence (R = radius of particle).[33] We compared the hydrodynamic diameter H_D of each sample based on the averaged peak value in intensity profiles after repeated measurement at different scattering angles. These are reported along with the standard deviation and the width of intensity profile from each sample in Table 1.

FRET Data Collection. Steady-state fluorescent spectra from solutions of dye-labeled DNA and QD–DNA bioconjugates were collected on a Tecan Safire Dual monochromator multifunction microtiter plate reader (Tecan, Research Triangle Park, NC, USA) using 475 nm excitation for FAM acceptors and 300 nm for QD donors. For each QD–dye or dye–dye donor–acceptor pair, the Förster distance R_0 corresponding to a donor–acceptor separation resulting in 50% energy transfer efficiency was calculated using the expression[58]

$$R_0 = 9.78 \times 10^3 [k^2 n^{-4} Q_D J(\lambda)]^{1/6} \quad (3)$$

where n is the refractive index of the medium, Q_D is the PL quantum yield (QY) of the donor, $J(\lambda)$ is the spectral overlap integral, and κ^2 is the dipole orientation factor. We use a $\kappa^2 = 2/3$ value shown to be appropriate for the random dipole orientations found within these heterogeneous self-assembled configurations as detailed previously.[59] The average energy transfer efficiency E was extracted for each set of QD/dye–dye donor–acceptor conjugates using the expression:

$$E = \frac{(F_D - F_{DA})}{F_D} \quad (4)$$

where F_D and F_{DA} are, respectively, the fluorescence intensities of the donor alone and the donor in the presence of the acceptor(s). For the QD assembly, it is assumed that each construct exhibits, on average, a centrosymmetric distribution of acceptors characterized by relatively constant center-to-center separation distances r, where the energy transfer efficiency data can be fit to the expression[60]

$$E = \frac{n{R_0}^6}{n{R_0}^6 + r^6} \quad (5)$$

Here, n is the average number of acceptors per donor. The direct excitation contribution to each of the acceptors was estimated by assaying control samples prepared in the same manner either with an unlabeled spacer in place of the dye-labeled DNA or with the QD omitted from the assembly using the same excitation wavelength as the FRET configuration. These control spectra were utilized for deconvolution where appropriate. For conjugates self-assembled with small numbers of acceptors, the heterogeneity in conjugate valence was accounted for by using a Poisson distribution function, $p(N,n)$, during the fitting of the FRET efficiency data:[61]

$$E(n) = \sum_{k=1}^{\infty} p(k,n)\, E(k) \text{ and } p(k,n) = \frac{e^{-n} n^k}{k!} \quad (6)$$

where n is the average acceptor-to-QD ratio used during reagent mixing and k is the exact number of peptide-dye conjugated to the QD.

Acknowledgment. The authors thank M. Twigg and S. Trammel for assistance with the TEM imaging and the electrochemistry measurements and acknowledge ONR, NRL, NRL-NSI, DTRA, and DARPA for financial support.

Supporting Information Available: Chemical structures of the thiol and amine modifiers and dye labels along with the AuNP surface ligand and linker. Additionally, a representative processed AFM image and a corresponding plot from the pair correlation analysis applied to that image are provided. This information is available free of charge *via* the Internet at http://pubs.acs.org.

REFERENCES AND NOTES

1. Boeneman, K.; Deschamps, J. R.; Buckhout-White, S.; Prasuhn, D. E.; Blanco-Canosa, J. B.; Dawson, P. E.; Stewart, M. H.; Susumu, K.; Goldman, E. R.; Ancona, M.; *et al.* Quantum Dot DNA Bioconjugates: Attachment Chemistry Strongly Influences the Resulting Composite Architecture. *ACS Nano* **2010**, *4*, 7253–7266.
2. Mitchell, G. P.; Mirkin, C. A.; Letsinger, R. L. Programmed Assembly of DNA Functionalized Quantum Dots. *J. Am. Chem. Soc.* **1999**, *121*, 8122–8123.
3. Deng, Z. X.; Tian, Y.; Lee, S. H.; Ribbe, A. E.; Mao, C. D. DNA-Encoded Self-Assembly of Gold Nanoparticles into One-Dimensional Arrays. *Angew. Chem., Int. Ed.* **2005**, *44*, 3582–3585.
4. Sapsford, K. E.; Park, D.; Goldman, E. R.; Foos, E. E.; Trammell, S. A.; Lowy, D. A.; Ancona, M. G. Selective DNA-Mediated Assembly of Gold Nanoparticles on Electroded Substrates. *Langmuir* **2008**, *24*, 10245–10252.
5. Seeman, N. C. An Overview of Structural DNA Nanotechnology. *Mol. Biotechnol.* **2007**, *37*, 246–257.
6. Kolaric, B.; Vallee, R. A. L. Dynamics and Stability of DNA Mechano-Nanostructures: Energy-Transfer Investigations. *J. Phys. Chem. C* **2010**, *114*, 10670–10670.
7. Sacca, B.; Meyer, R.; Feldkamp, U.; Schroeder, H.; Niemeyer, C. M. High-Throughput, Real-Time Monitoring of the Self-Assembly of DNA Nanostructures by FRET Spectroscopy. *Angew. Chem., Int. Ed.* **2008**, *47*, 2135–2137.
8. Varghese, R.; Wagenknecht, H. A. DNA as a Supramolecular Framework for the Helical Arrangements of Chromophores: Towards Photoactive DNA-Based Nanomaterials. *Chem. Commun.* **2009**, 2615–2624.
9. Li, H. Y.; Park, S. H.; Reif, J. H.; LaBean, T. H.; Yan, H. DNA-Templated Self-Assembly of Protein and Nanoparticle Linear Arrays. *J. Am. Chem. Soc.* **2004**, *126*, 418–419.
10. Wilner, O. I.; Weizmann, Y.; Gill, R.; Lioubashevski, O.; Freeman, R.; Willner, I. Enzyme Cascades Activated on Topologically Programmed DNA Scaffolds. *Nat. Nanotechnol.* **2009**, *4*, 249–254.
11. Rothemund, P. W. K. Folding DNA to Create Nanoscale Shapes and Patterns. *Nature* **2006**, *440*, 297–302.
12. Steinhauer, C.; Jungmann, R.; Sobey, T. L.; Simmel, F. C.; Tinnefeld, P. DNA Origami as a Nanoscopic Ruler for Super-Resolution Microscopy. *Angew. Chem., Int. Ed.* **2009**, *48*, 8870–8873.
13. Pal, S.; Deng, Z. T.; Ding, B. Q.; Yan, H.; Liu, Y. DNA-Origami-Directed Self-Assembly of Discrete Silver-Nanoparticle Architectures. *Angew. Chem., Int. Ed.* **2010**, *49*, 2700–2704.
14. Shen, W. Q.; Zhong, H.; Neff, D.; Norton, M. L. NTA Directed Protein Nanopatterning on DNA Origami Nanoconstructs. *J. Am. Chem. Soc.* **2009**, *131*, 6660–6661.
15. Kuzuya, A.; Kimura, M.; Numajiri, K.; Koshi, N.; Ohnishi, T.; Okada, F.; Komiyama, M. Precisely Programmed and Robust 2D Streptavidin Nanoarrays by Using Periodical Nanometer-Scale Wells Embedded in DNA Origami Assembly. *Chembiochem* **2009**, *10*, 1811–1815.
16. Kuzyk, A.; Laitinen, K. T.; Torma, P. DNA Origami as a Nanoscale Template for Protein Assembly. *Nanotechnology* **2009**, *20*, 235305.
17. Wang, T.; Sha, R.; Birktoft, J.; Zheng, J.; Mao, C.; Seeman, N. C. A DNA Crystal Designed to Contain Two Molecules per Asymmetric Unit. *J. Am. Chem. Soc.* **2010**, *132*, 15471–15473.
18. Becerril, H. A.; Ludtke, P.; Willardson, B. M.; Woolley, A. T. DNA-Templated Nickel Nanostructures and Protein Assemblies. *Langmuir* **2006**, *22*, 10140–10144.
19. Sapsford, K. E.; Tyner, K. M.; Dair, B. J.; Deschamps, J. R.; Medintz, I. L. Analyzing Nanomaterial Bioconjugates: A Review of Current and Emerging Purification and Characterization Techniques. *Anal. Chem.* **2011**, *83*, 4453–4488.
20. Feng, X. Z.; Bash, R.; Balagurumoorthy, P.; Lohr, D.; Harrington, R. E.; Lindsay, S. M. Conformational Transition

in DNA on a Cold Surface. *Nucleic Acids Res.* **2000**, *28*, 593–596.
21. Sindbert, S.; Kalinin, S.; Nguyen, H.; Kienzler, A.; Clima, L.; Bannwarth, W.; Appel, B.; Muller, S.; Seidel, C. A. M. Accurate Distance Determination of Nucleic Acids *via* Förster Resonance Energy Transfer: Implications of Dye Linker Length and Rigidity. *J. Am. Chem. Soc.* **2011**, *133*, 2463–2480.
22. Seeman, N. C. DNA Engineering and its Application to Nanotechnology. *Trends Biotechnol.* **1999**, *17*, 437–443.
23. Furrer, P.; Bednar, J.; Stasiak, A. Z.; Katritch, V.; Michoud, D.; Stasiak, A.; Dubochet, J. Opposite Effect of Counterions on the Persistence Length of Nicked and Non-Nicked DNA. *J. Mol. Biol.* **1997**, *266*, 711–721.
24. Protozanova, E.; Yakovchuk, P.; Frank-Kamenetskii, M. D. Stacked-Unstacked Equilibrium at the Nick Site of DNA. *J. Mol. Biol.* **2004**, *342*, 775–785.
25. Williams, R. C. Use of Polylysine for Adsorption of Nucleic-Acids and Enzymes to Electron-Microscope Specimen Films. *Proc. Natl. Acad. Sci. U. S. A.* **1977**, *74*, 2311–2315.
26. Murakami, M.; Kanda, R.; Minamihisamatsu, M.; Hayata, I. Characterization of Ionizing Radiation-Induced Ring Chromosomes by Atomic Force Microscopy. *Anal. Biochem.* **2004**, *334*, 251–256.
27. Hajibagheri, M. A. N. Visualization of DNA and RNA Molecules, and Protein-DNA Complexes for Electron Microscopy. *Mol. Biotechnol.* **2000**, *15*, 167–184.
28. Griffith, J. D.; Lee, S.; Wang, Y. H. Visualizing Nucleic Acids and Their Complexes Using Electron Microscopy. *Curr. Opin. Struct. Biol.* **1997**, *7*, 362–366.
29. Markiewicz, P.; Goh, M. C. Atomic-Force Microscope Tip Deconvolution Using Calibration Arrays. *Rev. Sci. Instrum.* **1995**, *66*, 3186–3190.
30. Bombelli, F. B.; Gambinossi, F.; Lagi, M.; Berti, D.; Caminati, G.; Brown, T.; Sciortino, F.; Norden, B.; Baglioni, P. DNA Closed Nanostructures: A Structural and Monte Carlo Simulation Study. *J. Phys. Chem. B* **2008**, *112*, 15283–15294.
31. Oh, E.; Susumu, K.; Blanco-Canosa, J. B.; Medintz, I. L.; Dawson, P. E.; Mattoussi, H. Preparation of Stable Maleimide-Functionalized Au Nanoparticles and Their Use in Counting Surface Ligands. *Small* **2010**, *6*, 1273–1278.
32. Hill, H. D.; Millstone, J. E.; Banholzer, M. J.; Mirkin, C. A. The Role Radius of Curvature Plays in Thiolated Oligonucleotide Loading on Gold Nanoparticles. *ACS Nano* **2009**, *3*, 418–424.
33. Brown, W. *Dynamic Light Scattering: The Method and Some Applications*; Clarendon Press: Oxford: New York, 1993.
34. Tinland, B.; Pluen, A.; Sturm, J.; Weill, G. Persistence Length of Single-Stranded DNA. *Macromolecules* **1997**, *30*, 5763–5765.
35. Nedelcu, S.; Slater, G. W. Branched Polymeric Labels Used as Drag-Tags in Free-Solution Electrophoresis of ssDNA. *Electrophoresis* **2005**, *26*, 4003–4015.
36. Falabella, J. B.; Cho, T. J.; Ripple, D. C.; Hackley, V. A.; Tarlov, M. J. Characterization of Gold Nanoparticles Modified with Single-Stranded DNA Using Analytical Ultracentrifugation and Dynamic Light Scattering. *Langmuir* **2010**, *26*, 12740–12747.
37. Didenko, V. V. DNA Probes Using Fluorescence Resonance Energy Transfer (FRET): Designs and Applications. *Biotechniques* **2001**, *31*, 1106–1116.
38. Sapsford, K. E.; Pons, T.; Medintz, I. L.; Higashiya, S.; Brunel, F. M.; Dawson, P. E.; Mattoussi, H. Kinetics of Metal-Affinity Driven Self-Assembly Between Proteins or Peptides and CdSe-ZnS Quantum Dots. *J. Phys. Chem. C* **2007**, *111*, 11528–11538.
39. Medintz, I. L.; Mattoussi, H. Quantum Dot-Based Resonance Energy Transfer and its Growing Application in Biology. *Phys. Chem. Chem. Phys.* **2009**, *11*, 17–45.
40. Zhang, C. Y.; Johnson, L. W. Quantum-Dot-Based Nanosensor for RRE IIB RNA-Rev Peptide Interaction Assay. *J. Am. Chem. Soc.* **2006**, *128*, 5324–5325.
41. Nazarenko, I.; Pires, R.; Lowe, B.; Obaidy, M.; Rashtchian, A. Effect of Primary and Secondary Structure of Oligodeoxyribonucleotides on the Fluorescent Properties of Conjugated Dyes. *Nucleic Acids Res.* **2002**, *30*, 2089–2095.
42. He, Y.; Ye, T.; Su, M.; Zhang, C.; Ribbe, A. E.; Jiang, W.; Mao, C. D. Hierarchical Self-Assembly of DNA into Symmetric Supramolecular Polyhedra. *Nature* **2008**, *452*, 198–U41.
43. Geissler, D.; Charbonniere, L. J.; Ziessel, R. F.; Butlin, N. G.; Lohmannsroben, H. G.; Hildebrandt, N. Quantum Dot Biosensors for Ultrasensitive Multiplexed Diagnostics. *Angew. Chem., Int. Ed.* **2010**, *49*, 1396–1401.
44. Morgner, F.; Geissler, D.; Stufler, S.; Butlin, N. G.; Lohmannsroben, H. G.; Hildebrandt, N. A Quantum-Dot-Based Molecular Ruler for Multiplexed Optical Analysis. *Angew. Chem., Int. Ed.* **2010**, *49*, 7570–7574.
45. Algar, W. R.; Susumu, K.; Delehanty, J. B.; Medintz, I. L. Semiconductor Quantum Dots in Bioanalysis: Crossing the Valley of Death. *Anal. Chem.* **2011**, *83*, 8826–8837.
46. Macke, T.; Case, D. A. Modeling Unusual Nucleic Acid Structures. In *Molecular Modeling of Nucleic Acids*; Leontes, N. B. Santa Lucia, J., Jr., Ed.; American Chemical Society: Washington, DC, 1998; pp 379−393.
47. Medintz, I. L.; Clapp, A. R.; Brunel, F. M.; Tiefenbrunn, T.; Uyeda, H. T.; Chang, E. L.; Deschamps, J. R.; Dawson, P. E.; Mattoussi, H. Proteolytic Activity Monitored by Fluorescence Resonance Energy Transfer Through Quantum-Dot-Peptide Conjugates. *Nat. Mater.* **2006**, *5*, 581–589.
48. Pettersen, E. F.; Goddard, T. D.; Huang, C. C.; Couch, G. S.; Greenblatt, D. M.; Meng, E. C.; Ferrin, T. E. UCSF Chimera−A Visualization Aystem for Exploratory Research and Analysis. *J. Comput. Chem.* **2004**, *25*, 1605–1612.
49. Wang, J.; Wang, W.; Kollman, P. A.; Case, D. A. Automatic Atom Type and Bond Type Perception in Molecular Mechanical Calculations. *J. Mol. Graphics* **2006**, *25*, 247–260.
50. Prasuhn, D. E., Jr. Development of Icosahedral Virus Particles as Multivalent Display Scaffolds for Metal Complexes. PhD Thesis. Scripps Resesarch Institute, La Jolla, CA, 2007.
51. Peng, Z. A.; Peng, X. Formation of High-Quality CdTe, CdSe, and CdS Nanocrystals Using CdO as Precursor. *J. Am. Chem. Soc.* **2001**, *123*, 183–184.
52. Prashun, D. E.; Blanco-Canosa, J. B.; Vora, G. J.; Delehanty, J. B.; Susumu, K.; Mei, B. C.; Dawson, P. E.; Mattoussi, H.; Medintz, I. L. Combining Chemoselective Ligation with Polyhistidine-Driven Self-Assembly for the Modular Display of Biomolecules on Quantum Dots. *ACS Nano* **2010**, *4*, 267–78.
53. Dirksen, A.; Dawson, P. E. Rapid Oxime and Hydrazone Ligations with Aromatic Aldehydes for Biomolecular Labeling. *Bioconjugate Chem.* **2008**, *19*, 2543–2548.
54. Sapsford, K. E.; Farrell, D.; Sun, S.; Rasooly, A.; Mattoussi, H.; Medintz, I. L. Monitoring of Enzymatic Proteolysis on a Electroluminescent-CCD Microchip Platform Using Quantum Dot-Peptide Substrates. *Sens. Actuators, B* **2009**, *139*, 13–21.
55. Herne, T. M.; Tarlov, M. J. Characterization of DNA Probes Immobilized on Gold Surfaces. *J. Am. Chem. Soc.* **1997**, *119*, 8916–8920.
56. Horcas, I.; Fernandez, R.; Gomez-Rodriguez, J. M.; Colchero, J.; Gomez-Herrero, J.; Baro, A. M. WSXM: A Software for Scanning Probe Microscopy and a Tool for Nanotechnology. *Rev. Sci. Instrum.* **2007**, *78*, 013705.
57. Crocker, J. C.; Grier, D. G. Methods of Digital Video Microscopy for Colloidal Studies. *J. Colloid Interface Sci.* **1996**, *179*, 298–310.
58. Lakowicz, J. R. *Principles of Fluorescence Spectroscopy*, Third ed.; Springer: New York, 2006.
59. Medintz, I. L.; Konnert, J. H.; Clapp, A. R.; Stanish, I.; Twigg, M., E.; Mattoussi, H.; Mauro, J. M.; Deschamps, J. R. A Fluorescence Resonance Energy Transfer Derived Structure of a Quantum Dot-Protein Bioconjugate Nanoassembly. *Proc. Natl. Acad. Sci. U. S. A.* **2004**, *101*, 9612–9617.
60. Clapp, A. R.; Medintz, I. L.; Mauro, J. M.; Fisher, B. R.; Bawendi, M. G.; Mattoussi, H. Fluorescence Resonance Energy Transfer Between Quantum Dot Donors and Dye-Labeled Protein Acceptors. *J. Am. Chem. Soc.* **2004**, *126*, 301–310.
61. Pons, T.; Medintz, I. L.; Wang, X.; English, D. S.; Mattoussi, H. Solution-Phase Single Quantum Dot Fluorescence Resonant Energy Transfer Sensing. *J. Am. Chem. Soc.* **2006**, *128*, 15324–15331.